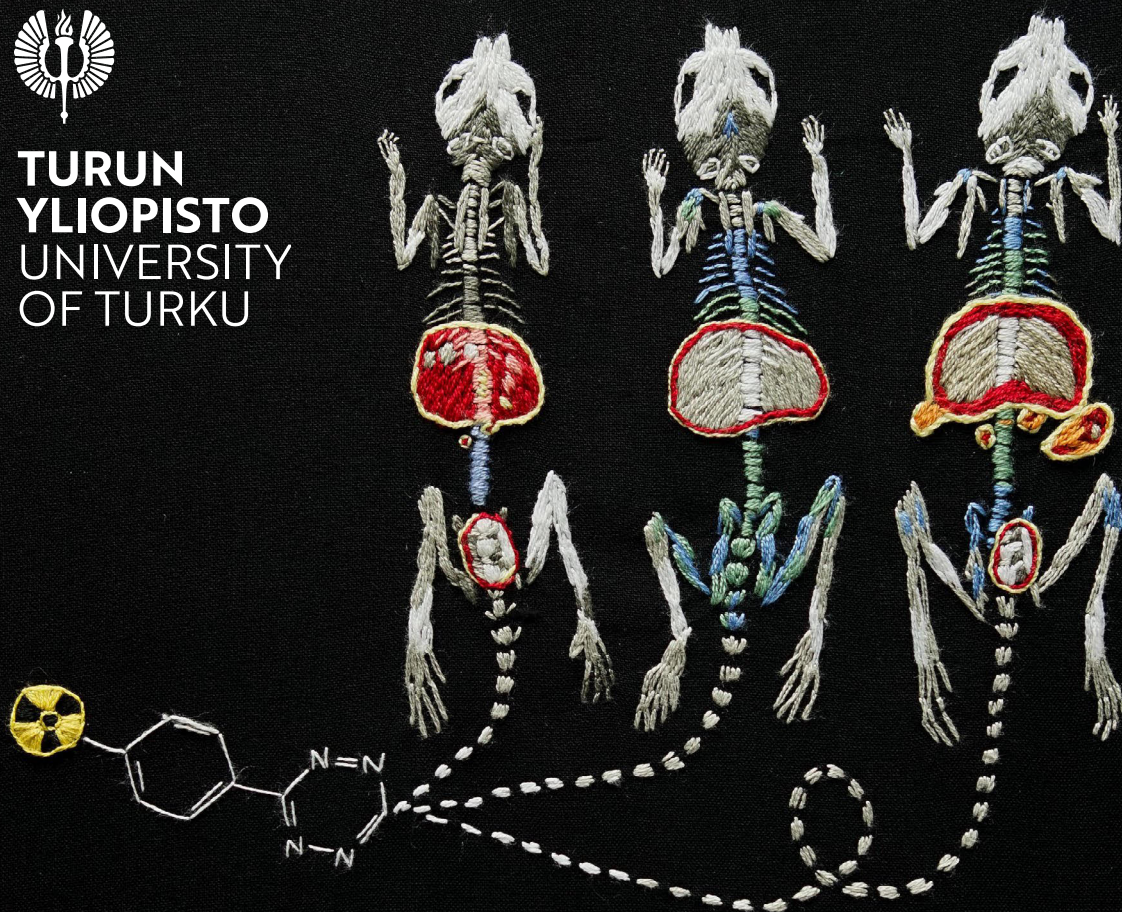TURUN
YLIOPISTO
UNIVERSITY
OF TURKU

RADIOLABELING OF SPHERICAL OLIGONUCLEOTIDES FOR TARGETED AND PRETARGETED PET IMAGING

Biological evaluation of structural effects by using a tetrazine [^{18}F]fluoroglycoconjugate

Tatsiana Auchynnikava

RADIOLABELING OF SPHERICAL OLIGONUCLEOTIDES FOR TARGETED AND PRETARGETED PET IMAGING

Biological evaluation of structural effects
by using a tetrazine [^{18}F]fluoroglycoconjugate

Tatsiana Auchynnikava

University of Turku

Faculty of Science
Department of Chemistry
Radiopharmaceutical Chemistry
Drug Research Doctoral Programme

Supervised by

Professor Anu J. Airaksinen, PhD
Department of Chemistry and
Turku PET Centre
University of Turku
Turku, Finland

Assistant Professor Xiang-Guo Li, PhD
Department of Chemistry and
Turku PET Centre
University of Turku
Turku, Finland

Reviewed by

Professor Tapani Viitala, PhD
Faculty of Science and
Engineering/Faculty of Pharmacy
Åbo Akademi/University of Helsinki
Turku/Helsinki, Finland

Assistant Professor Umberto Battisti, PhD
Department of Drug Design and
Pharmacology
University of Copenhagen
Copenhagen, Denmark

Opponent

Assistant Professor Verena Pichler, PhD
Department of Pharmaceutical Sciences
University of Vienna
Vienna, Austria

Cover Image: Tatsiana Auchynnikava

To family, friends, and furry friends

UNIVERSITY OF TURKU
Faculty of Science
Department of Chemistry
Radiopharmaceutical Chemistry
TATSIANA AUCHYNNIKAVA: Radiolabeling of spherical oligonucleotides for targeted and pretargeted PET imaging. Biological evaluation of structural effects by using a tetrazine [18F]fluoroglycoconjugate.
Doctoral Dissertation, 138 pp.
Drug Research Doctoral Programme
June 2024

ABSTRACT

Positron emission tomography (PET) is a sensitive and non-invasive molecular imaging modality with various applications, including drug discovery and the development of novel therapeutics evaluation at an early stage. Pretargeted PET offers a solution for studying processes with slow pharmacokinetics using short-lived radionuclides. Such an approach decreases the radiation burden for the subject and improves target-to-non-target contrast. Spherical nucleic acids (SNA) represent the emerging alternative nanostructures of nucleic acid-based delivery agents of therapeutic oligonucleotides (ONs). SNAs have a range of benefits over linear ONs, however, the behavior of these structures *in vivo* requires thorough investigation.

Our aim was to develop radiolabeling methods for molecular SNA (MSNA) in both targeted and pretargeted PET imaging; this method was then used to study the structural effect on MSNA *in vivo* biodistribution in tumor-bearing mice. In the study, 2-[18F]fluoro-2-deoxy-*D*-glucose conjugated tetrazine ([18F]FDG-Tz) was first evaluated as a potential pretargeted agent in healthy mice using dynamic PET imaging, and then utilized for direct and pretargeted radiolabeling of MSNAs. This allowed the following to be studied: the influence of backbone chemistry, and the folate decoration and *trans*-cyclooctene (TCO)-load percentage on the biodistribution in tumor-beating mice with targeted and pretargeted PET. The results demonstrated suitability of [18F]FDG-Tz for direct and pretargeted labeling of MSNAs. MSNAs exhibited favorable biodistribution compared to linear, single-stranded ON. In addition, the pretargeted approach showed the highest tumor uptake compared to directly labeled MSNA.

In conclusion, [18F]FDG-Tz successfully enabled the radiolabeling of MSNA for both targeted and pretargeted approaches, facilitating the evaluation of structural effects on MSNA biodistribution.

KEYWORDS: PET, click chemistry, IEDDA, tetrazine, [18F]FDG, bioorthogonal chemistry, pretargeted PET, molecular spherical nucleic acids.

TURUN YLIOPISTO
Matemaattis-luonnontieteellinen tiedekunta
Kemian laitos
Radiofarmaseuttinen kemia
TATSIANA AUCHYNNIKAVA: Pallonukleiinihappojen radioleimaus esikoh-
dennettua ja kohdennettua PET-kuvantamista varten. Rakenteellisten muu-
toksien vaikutuksen arviointi tetratsiini-[18F]fluoroglykokonjugaatin avulla.
Väitöskirja, 138 s.
Lääketutkimuksen tohtoriohjelma
Kesäkuu 2024

TIIVISTELMÄ

Positroniemissiotomografia (PET) on herkkä ja kajoamaton molekyylitason kuvanta-
mismenetelmä, jolla on monia sovelluksia, joihin kuuluvat muun muassa lääkekehitys
sekä uusien terapeuttisten menetelmien arviointi tutkimuksen varhaisessa vaiheessa.
Esikohdennettu PET tarjoaa ratkaisun biologisesti hitaampien farmakokineettisten
prosessien tutkimiseen lyhytikäisten radionuklidien avulla. Lisäksi se vähentää
potilaan säteilyaltistusta ja parantaa kuvattavan biologisen kohteen kontrastia PET-
kuvissa. Tutkimuksen kohteena olevat pallonukleiinihapot ovat nouseva vaihtoehto
nukleiinihappopohjaisille terapeuttisille oligonukleotideille. Pallonukleiinihapot
tarjoavat useita etuja verrattuna lineaarisiin oligonukleotideihin, mutta näiden
rakenteiden käyttäytymistä elimistössä on tutkittava perusteellisesti.

Tavoitteenamme oli kehittää uusia menetelmiä molekyylisten pallonukleiinihap-
pojen kohdennettuun ja esikohdennettuun PET-kuvantamiseen. Kehitettyjä menetel-
miä käytettiin tutkimaan pallonukleiinihappojen rakenteen vaikutusta *in vivo* bio-
distribuutioon syöpäkasvaimia kantavissa hiirissä. Tutkimuksessa 2-[18F]fluoro-2-
deoksi-*D*-glukoosi konjugoitua tetratsiinia ([18F]FDG-Tz)-merkkiainetta arvioitiin
ensin potentiaalisena esikohdentavana PET-merkkiaineena, jonka jälkeen merkki-
ainetta käytettiin sekä suoraan, että esikohdennettuna pallonukleiinihappojen radio-
leimaukseen. Tämä mahdollisti oligonukleotidien selkärangan kemian, foolihappo-
konjugaation sekä *trans*-syklookteenimodifikaatioiden määrän vaikutuksien tutkimi-
sen biodistribuution. Tulokset osoittivat [18F]FDG-Tz:n soveltuvan pallonukleiini-
happojen suoraan ja esikohdennettuun radioleimaukseen. Pallonukleiinihappojen
biodistribuutio osoittautui suotuisammaksi lineaarisiin oligonukleotideihin verrattu-
na. Lisäksi esikohdennettu lähestymistapa tuotti korkeamman kertymän kasvaimiin
verrattuna suoraan radioleimattuihin pallonukleiinihappoihin.

Yhteenvetona [18F]FDG-Tz mahdollisti onnistuneesti molekyylisten pallonukleii-
nihappojen radioleimauksen sekä kohdennettua että esikohdennettua lähestymistapaa
käyttäen. Kehitetyt menetelmät helpottavat rakenteellisten vaikutusten arviointia
pallonukleiinihappojen biodistribuutiotutkimuksessa.

ASIASANAT: PET, klikkikemia, IEDDA, tetratsiini, [18F]FDG, bioortogonaalinen
kemia, esikohdennettu PET-kuvantaminen, molekyylinen pallonukleiinihappo.

Table of Contents

Abbreviations

%ID/g	percentage injected dose per gram of tissue
ACN	acetonitrile
BCN	bicyclononyne
CuAAC	copper(I)-catalyzed azide-alkyne cycloaddition
CT	computer tomography
DBCO	dibenzocyclooctyl
DMSO	dimethyl sulfoxide
DNA	deoxyribonucleic acid
EOB	end of bombardment
EOS	end of synthesis
FBS	fetal bovine serum
FDG	2-fluoro-2-deoxy-D-glucose
FDR	5-fluoro-5-deoxy-D-ribose
FR	folate receptor
GLUT1	glucose transporter 1
GMP	good manufacturing practice
H&E	hematoxylin and eosin
HER2	human epidermal growth factor receptor 2
HPLC	high-performance liquid chromatography
IEDDA	inverse electron demand Diels–Alder reaction
EPR	enhanced permeability and retention
LC-MS/MS	liquid chromatography-tandem mass spectrometry
L.I.	large intestine
LUMO	lowest unoccupied molecular orbital
MALS	multiple angle light scattering detector
MPS	mononuclear phagocyte system
MRI	magnetic resonance imaging
mRNA	messenger RNA
MSNA	molecular spherical nucleic acids
NMR	nuclear magnetic resonance
NOTA	1,4,7-triazacyclononane-1,4,7-triacetic acid

ON	oligonucleotide
PAGE	polyacryl amide gel electrophoresis
PBS	phosphate-buffered saline
PET	positron emission tomography
PMO	phosphorodiamidate morpholino oligomer
PNA	peptide nucleic acid
PO	phosphodiester
POS	3-phenyl 1,2,4-dithiazoline-5-one
PS	phosphorothioate
QMA	quaternary methyl ammonium
RCP	radiochemical purity
RCY	radiochemical yield
RES	reticuloendothelial system
RNA	ribonucleic acid
RNase	ribonuclease
ROI	region of interest
r.t.	room temperature
SEC	size-exclusion chromatography
S.I.	small intestine
SiFA	silicon-fluoride acceptor
S.M.	skeleton muscle
SNA	spherical nucleic acids
SPAAC	strain-promoted azide-alkyne cycloaddition
SPE	solid phase extraction
SEC-MALS	size-exclusion chromatography equipped with multi-angle light scattering detector
SPECT	single photon emission computer tomography
SuFEx	sulfur fluoride exchange
SUV	standardized uptake value
TAC	time-activity curves
TBAOH	tetrabutylammoiumhydroxide
TCO	*trans*-cyclooctene
TFA	trifluoroacetic acid
TLC	thin-layer chromatography

List of Original Publications

This dissertation is based on the following original publications, which are referred to in the text by their Roman numerals:

I   **Auchynnikava T.**, Äärelä A., Liljenbäck H., Järvinen J., Andriana P., Kovacs L., Rautio J., Rajander J., Virta P., Roivainen A., Li X. G., Airaksinen A. Tetrazine Glycoconjugate for Pretargeted Positron Emission Tomography Imaging of *trans*-Cyclooctene-Functionalized Molecular Spherical Nucleic Acids. *ACS Omega*, 2023; 8(48): 45326-45336.

II   Äärelä A.*, **Auchynnikava T.***, Moisio O., Liljenbäck H., Andriana P., Iqbal I., Lehtimäki J., Rajander J., Salo H., Roivainen A., Airaksinen A., Virta P. *In Vivo* Imaging of [60]Fullerene-Based Molecular Spherical Nucleic Acids by Positron Emission Tomography. *Mol. Pharm*, 2023; 20(10): 5043-5051.

III **Auchynnikava T.***, Äärelä A.*, Moisio O., Liljenbäck H., Andriana P., Iqbal I., Laine T., Palani S., Lehtimäki J., Rajander J., Salo H., Airaksinen A., Virta P., Roivainen A. Biological evaluation of molecular spherical nucleic acids: targeting tumors via a hybridization-based folate decoration. **Submitted manuscript**.

The original publications have been reproduced with the permission of the copyright holders. *Equal contribution.

1   Introduction

1.1   Positron emission tomography

1.1.1   Principle of positron emission tomography

Positron emission tomography (PET) as a non-invasive functional molecular imaging technique is a valuable tool in clinical diagnostics for various conditions, including oncological, cardiological, infectious, and neurological diseases. It is also an instrument for monitoring treatment responses (Ametamey et al., 2008). Additionally, PET is widely utilized in drug discovery for both preclinical evaluation and early clinical evaluation of new drug candidates (Welch et al., 2021).

PET relies on the usage of imaging agents radiolabeled with radionuclides that decay via positron (β^+) emission. The emitted positron almost immediately collides with an electron due to interactions with the surrounding matter. Two 511 keV gamma rays are generated simultaneously, both of which are traveling in almost opposite direction (180°). Figure 1 represents this process, which is called annihilation (Cherry & Dahlbom, 2006).

PET scanners include a range of detectors, organized in the shape of a ring around the subject. The data reconstruction into a 3D image is based on the assumption that two gamma rays are released concurrently in opposite directions. A PET image is usually combined with computer tomography (CT) or magnetic resonance imaging (MRI) for anatomical reference, as PET provides functional or molecular data, which requires an additional source for anatomical localization of the processes.
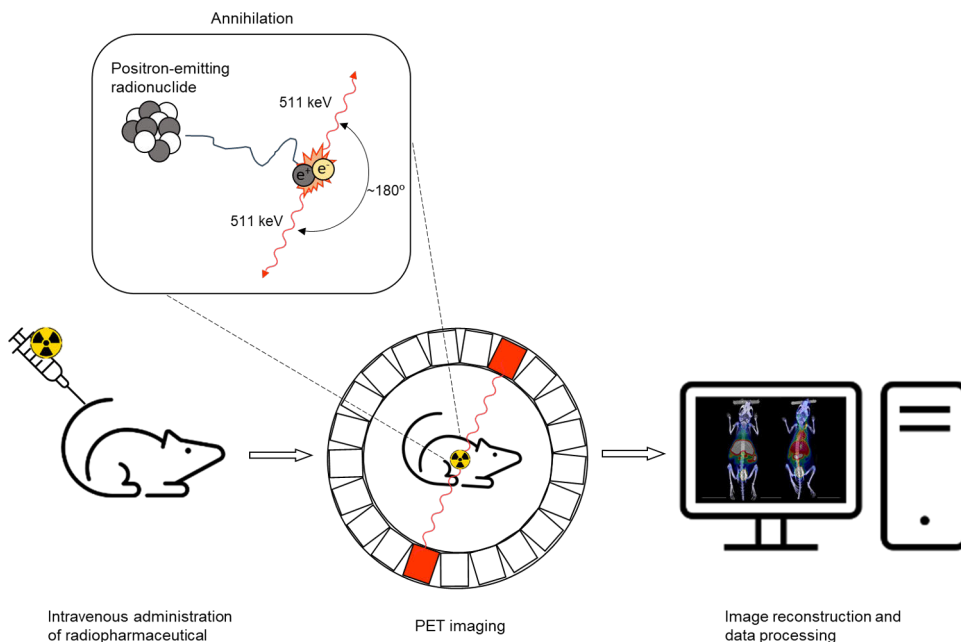
Figure 1. Principles of positron emission tomography.

1.1.2 Positron emitting radionuclides

The radionuclide selection relies on their unique physical properties, and requires careful consideration in order to achieve optimal images. Positron emitters do not perform pure β^+-decay. For example, fluorine-18 exhibits 96.9% β^+-decay with the remaining 3.1% being electron capture (Table 1). A higher percentage of β^+-decay is preferable due to the ability of detectors in PET scanners to detect only gamma rays. However, recent advancements in image reconstruction technologies have alleviated the concerns about none pure positron emitters. Although the lower β^+-decay percentage increases radiation doses.

Table 1. Physical properties of the commonly used positron emitters (Conti & Eriksson, 2016; *Laboratoire National Henri Becquerel*, n.d.).

Radionuclide	$T_{1/2}$	Type of decay	E_{max} (MeV)	Starting material	β^+-decay product
^{15}O	2.04 min	β^+ (99.9%)	1.732	$^{14}N(d,n)$	^{15}N
^{13}N	9.97 min	β^+ (99.8%)	1.199	$^{16}O(p,\alpha)$	^{13}C
^{11}C	20.4 min	β^+ (99.8%)	0.96	$^{14}N(p,\alpha)$	^{11}B
^{68}Ga	67.7 min	β^+ (88.9%)	1.899	^{68}Ge	^{68}Zn
^{18}F	109.8 min	β^+ (96.9%)	0.634	$^{18}O(p,n)$	^{18}O
^{89}Zr	78.4 h	β^+ (22.7%)	0.902	$^{89}Y(p,n)$	^{89}Y

* $T_{1/2}$ = half-life, E_{max} = maximum positron energy.

When selecting a positron emitter, considering the maximum positron energy is crucial. This property significantly impacts the image resolution, especially for imaging small subjects like rodents or specific targets in humans. The maximum positron energy determines the distance a positron travels in the matter before annihilating with an electron. Lower energy shortens this range, while higher energy increases the travel range. For an optimal resolution, lower positron energy is preferred, as PET detects only the place of annihilation. For instance, fluorine-18 exhibits an energy of 0.634 MeV and has in this respect an advantage over gallium-68, which has a higher energy of 1.899 MeV.

The half-life stands out as a critical and distinctive property in radiochemistry, requiring careful consideration in synthesis, imaging planning, and transportation. A shorter half-life proves advantageous for conducting multiple scans on the same subject within a day but requires on-site production. Conversely, a longer half-life provides flexibility for multi-step synthesis and various transportation options.

Additionally, the design of the targeting molecule has an influence on the radionuclide production. Positron-emitting radionuclides are incorporated into the molecule structure, specifically engineered to selectively target distinct processes within a living organism. Therefore, the half-life of the radionuclide should align with the half-life of the targeting moiety to ensure optimal efficacy.

1.1.3   Targeted and pretargeted PET

A conventional or targeted approach in radiopharmaceutical chemistry is based on radiolabeling a targeting molecule prior the administration. The half-lives of the radionuclide and the targeting agent in such an approach should be comparable to reach the target. This method is effective for processes with rapid pharmacokinetics. However, a dilemma emerges when dealing with processes with slow pharmacokinetics, particularly in the study of therapeutics like nanomaterials and antibodies. These substances exhibit prolonged biological half-lives, often extending to a range of days. This requires the use of long-lived radionuclides such as zirconium-89 (3.3 days), indium-111 (2.8 days), and iodine-124 (4.2 days) for direct targeted imaging. However, the extended circulation of the radioactive compound brings the challenge of exposing a patient to radiation for a prolonged duration, as well as providing unnecessary and unacceptable dose to healthy tissues (Altai et al., 2017; Handula et al., 2021). In addition, longer-lived radionuclides tend to exhibit a lower percentage of β^+ decay type, resulting in lower imaging quality (Stéen et al., 2018).

The pretargeted approach has emerged as an elegant solution to overcoming this challenge. The principle involves a separate application of the slow targeting molecule (primary agent) and the subsequent introduction of the short-lived radiotracer (secondary agent). In the first step, the targeting moiety is administered.

It is given a sufficient amount of time to accumulate in the desired region and clear from the blood stream and healthy tissues, which may take several days. The subsequent step involves the administration of the radiotracer, which rapidly binds to the primary agent (Figure 2). Splitting the process into two parts allows the use of short-lived and high positron-emitting radionuclides, which expressively reduces the radiation burden to the patient, improves target-to-non-target contrast and therapeutic efficiency, and minimizes the doses to non-target tissues. In some cases, the application of a clearing agent is needed to remove excess of the targeting agent from the blood.
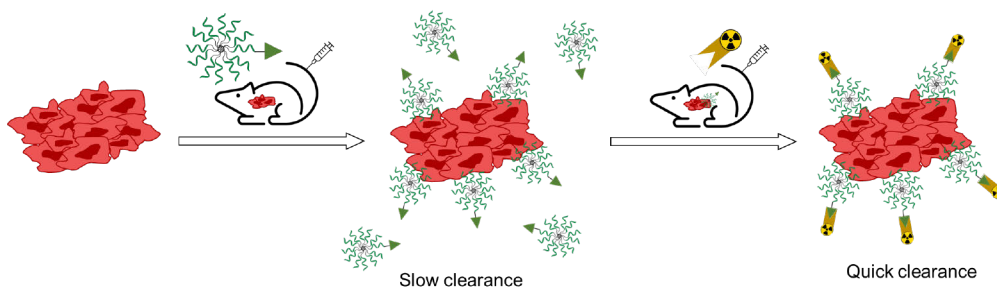
Figure 2. Principles of pretargeted positron emission tomography. Firstly, the targeting agent is administrated and given enough time to reach the target and clear from the blood, followed by the radiolabeled agent rapidly binding to the primary agent.

The pretargeted concept was first introduced almost 40 years ago (Reardan et al., 1985) and since then various strategies for recognition between targeting and imaging agents have been investigated. The main directions could be divided into non-covalent high-affinity interactions and covalent bond formations via bioorthogonal chemistry. In the first interaction type, the most common interactions are bispecific antibody and hapten recognition, streptavidin and biotin interactions, and hybridization on complementary oligonucleotides (ONs).

The first pretargeted imaging was conducted between the bispecific antibody and the radiolabeled hapten (Reardan et al., 1985). The bispecific antibody is designed with two different halves, enabling it to target two different antigens or their parts (epitopes) (Kontermann & Brinkmann, 2015). Despite an extensive number of studies and clinical translations (Goodwin et al., 1988; Karacay et al., 2011; McBride et al., 2006), this method faced limitations due to its low binding affinity between hapten and the bispecific antibody; this became the main drawback to a wide application of this approach.

Another pretargeted approach that has also been translated into clinical applications involves (strept)avidin and biotin interactions. In this method, the targeting agent can be functionalized either with (strept)avidin or biotin (Kalofonos
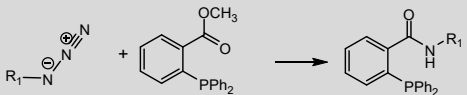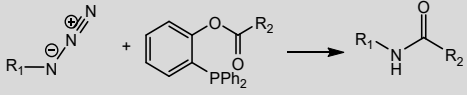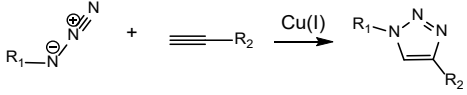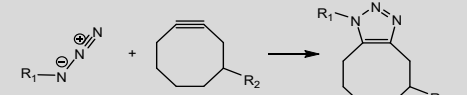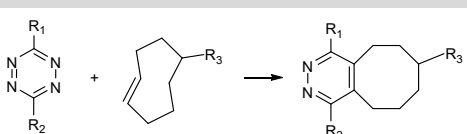
et al., 1990; Newton-Northup et al., 2009; Sakahara & Saga, 1999). Typically, (strept)avidin is applied to the target molecule in a pretargeted approach, while biotin is radiolabeled and utilized as a secondary agent. However, a concern rising from this specific method is its potential to block the binding sites of (strept)avidin, preventing effective interaction (Rusckowski et al., 1997). Although extensively studied and applied in clinics for the past 30 years, this method still has its drawbacks and is inferior to the bispecific antibody and hapten concept in terms of biodistribution profile and increased immunogenicity.

Hybridization on complementary ONs represents another non-covalent high-affinity interaction. It is based on Watson-Crick base pairing, facilitating the hybridization of ONs through hydrogen bonding. This approach requires modifications of the ONs to increase the stability towards *in vivo* nuclease degradation. This method was employed in preclinical pretargeted studies with antibodies, proteins, and peptides utilizing peptide nucleic acid (PNA) and phosphorodiamidate morpholino oligomers (PMOs) to overcome rapid *in vivo* nuclease degradation of the deoxyribonucleic acid (DNA)- or ribonucleic acid (RNA)-based oligomers (Amantana & Iversen, 2005; X. Li et al., 2015; Ray & Nordén, 2000). Recently, Affibody-mediated PNA-based pretargeting was used as the cotreatment with trastuzumab in human epidermal growth factor receptor 2 (HER2)-expressing tumor mice and showed an increased survival rate compared with only trastuzumab (Oroujeni et al., 2022).

Despite the previously mentioned approaches in pretargeted PET, including those that have found a clinical application, the most successful current option is covalent bond formations via bioorthogonal chemistry. Bioorthogonal chemistry covers a group of reactions occurring in the biological environment without causing interference. The reactions should be chemoselective, rapid, non-toxic, involve stable components at every step, and proceed under physiological conditions in an aqueous media. The most commonly used bioorthogonal reactions are presented in Table 2.

Initially, bioorthogonal chemistry emerged with the Staudinger ligation, forming an amine bond between an azide and a phosphine on the cell surface (Saxon & Bertozzi, 2000), and in later version with the traceless Staudinger ligation (Saxon et al., 2000). However, due to the slow *in vivo* reaction rate and *in vivo* phosphines oxidation, other bioorthogonal reactions have proven superior. Examples include strain-promoted azide-alkyne [3 + 2] cycloaddition (SPAAC) and tetrazine ligation. This has led to click chemistry, a term, introduced in 2001 by Kolb, Finn, and Sharpless (Kolb et al., 2001). This type of reaction needs to be fast, selective, not produce any by-products, and occur in aqueous or benign solutions. The definition of click chemistry broadly overlaps with conditions for bioorthogonal reactions, making it ideal for *in vivo* studies.

**Table 2.** Most commonly used bioorthogonal reactions.

Bioorthogonal reaction	Reaction scheme	Reaction rate k (M^{-1} s^{-1})	References
Staudinger ligation		10^{-3}	(Lin et al., 2005; Wang et al., 2015)
	"Traceless":	7.7×10^{-3}	(Soellner et al., 2006)
CuAAC		10-200	(Ji et al., 2012; Wang et al., 2015)
SPAAC		0.01-1	(Debets et al., 2014; Fehr et al., 2023)
IEDDA		$1-10^6$	(Blackman et al., 2008; Handula et al., 2021; Keinänen et al., 2016; Rossin et al., 2010)

The era of click chemistry began with Cu-catalyzed azide-alkyne [3 + 2] cycloaddition (CuAAC) (Kolb et al., 2001; Tornøe et al., 2002). It is based on the [3 + 2] cycloaddition between azides and alkynes (Huisgen, 1963), which, however, requires high temperatures and produces two regioisomers. The addition of a copper catalyst can address these issues giving only 1,4-disubstituted regioisomers at room temperature (W. Lee et al., 2021; Meldal & Diness, 2020). However, the use of Cu(I) is limited because of its toxicity and reactivity when using biomolecules, thus restricting its *in vivo* applications (Stéen et al., 2018). A water soluble Cu(I) ligand has been reported to promote the cycloaddition reaction rapidly without apparent toxicity for imaging of fucosylated glycans in developing zebrafish embryos (Soriano Del Amo et al., 2010).

To overcome the cytotoxicity of copper the introduction of a strained alkyne led to the development and application of SPAAC in pretargeted imaging (Agard et al., 2004; D. E. Lee et al., 2013; S. B. Lee et al., 2013). The benefit of this reaction is the absence of a catalyst and that it occurs under physiological conditions. However, the shortcoming of SPAAC is the potential reactivity of cyclooctyne ring with

nucleophiles in biological environment and slow kinetics. Despite these limitations, few compelling studies have been reported. Au et al. introduced a pretargeted nanoradioimmunotherapy strategy for the treatment of Non-Hodgkin lymphoma using a dibenzocyclooctyl (DBCO)-functionalized anti-CD20 antibody (α-CD20) and an azide-and yttrium-90 dual-functionalized dendrimer. This strategy increases the median survival time and has demonstrated tumor regression in xenograft models (Au et al., 2018).

The most optimal bioorthogonal reaction for the pretargeted PET imaging is the inverse electron demand Diels–Alder reaction (IEDDA), known for its superior reaction rates reaching up to $10^{6\text{-}7}$ $M^{-1}s^{-1}$ (Blackman et al., 2008). The IEDDA reaction mechanism involves two steps (Figure 3). The first step, which also determines the rate, is the [4 + 2] cycloaddition between an electron-poor diene, and an electron-rich dienophile (alkene or alkyne), followed by a retro Diels-Alder reaction (Oliveira et al., 2017).
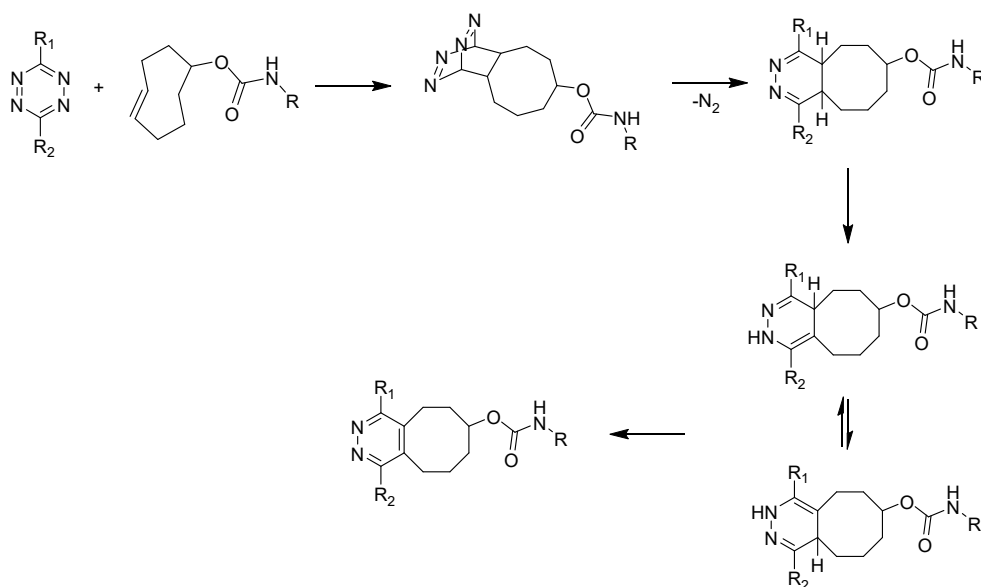
Figure 3. Mechanism of the IEDDA reaction between tetrazine and *trans*-cyclooctene.

The most common diene utilized in pretargeted studies is tetrazine. However, its structure should be carefully chosen, as various factors impact the reaction. Substitutions strongly influence reactivity, requiring a compromise between reactivity and stability since their stability inversely correlates with reactivity (Meyer et al., 2017; Rossin et al., 2010). In general, electron-withdrawing groups tend to increase reactivity by reducing the energy of the lowest unoccupied molecular orbital

(LUMO). Figure 4A represents the reactivity of different tetrazine scaffolds (García-Vázquez, Battisti, et al., 2022; Knall & Slugovc, 2013; Stéen et al., 2018). However, this limitation can be overcome by considering the distortion of the tetrazine caused by intramolecular repulsive N-N interaction when designing tetrazine (Svatunek et al., 2022).

Regarding electron-rich dienophiles, one of the first used in pretargeted experiments was norbornene (Devaraj et al., 2008). However, due to its slow kinetics, research progressed towards *trans*-cyclooctene (TCO), which is currently the most used dienophile for pretargeted IEDDA reaction (Keinänen et al., 2019; Keinänen, Fung, et al., 2017; Rossin et al., 2010). The reactivity of TCO is influenced by its structure (Figure 4B) (García-Vázquez, Jørgensen, et al., 2022), with *in vivo* deactivation possible through isomerization towards *cis*-cyclooctene.
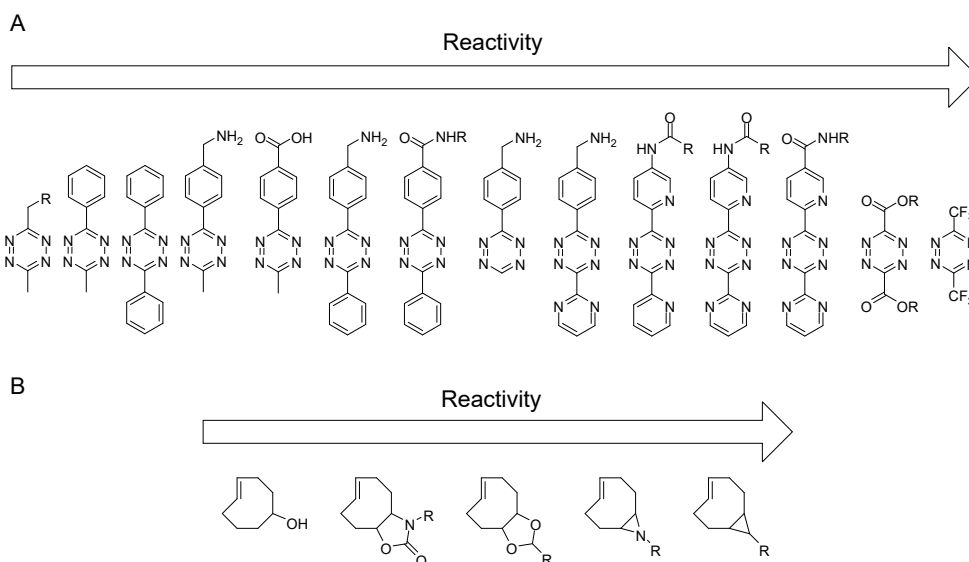
Figure 4. Reactivity of tetrazine scaffolds (A). Reactivity of different TCOs (B).

In addition to structural considerations, both TCO and tetrazine are vulnerable to harsh reaction conditions. TCO is photosensitive, and tetrazine is sensitive to basic conditions, posing challenges for fluorination and necessitating alternative approaches, which will be discussed in the next chapter.

The first pretargeted single photon emission computer tomography (SPECT) studies in mice utilizing IEDDA were conducted using ^{111}In-labeled tetrazine with TCO-functionalized monoclonal antibodies. The described method successfully targeted and visualized a colorectal tumor, while the radiotracer exhibited rapid urinary clearance (Rossin et al., 2010). Since then, pretargeted PET has been

extensively tested in numerous experiments involving nanomaterials and antibodies. Meyer et al. used a TCO-bearing antibody immunoconjugate and fluoridealuminum ([^{18}F]F-Al) with 1,4,7-triazacyclononane-1,4,7-triacetic acid (NOTA) (Al[^{18}F]NOTA)-labeled tetrazine for pretargeted imaging of expressing pancreatic cancer xenografts. Their approach demonstrated effective tumor detection with significant activity concentrations up to 6.4% ID/g at 4 hours after injection of the radioligand, together with dosimetric advantages (Meyer et al., 2016). Houghton et al. investigated IEDDA pretargeted imaging in radioimmunotherapy. ^{177}Lu-labeled tetrazine-bearing radioligand paired with TCO-modified 5B1-mAb showed rapid and persistent uptake in tumors and therapeutic response of preclinical murine models of pancreatic cancer (Houghton et al., 2017). Due to prolonged blood circulation of the nanoparticles, various types were *in vivo* radiolabeled in preclinical studies. Non-toxic and biodegradable TCO-modified mesoporous silicon nanoparticles were highlighted in pretargeted PET studies with 5-[^{18}F]fluoro-5-deoxy-*D*-ribose ([^{18}F]FDR) labeled tetrazine ([^{18}F]FDR-Tz) in a rapid IEDDA reaction (Keinänen, Mäkilä, et al., 2017). Nanomaterials play a considerable role as delivery agents, and supramolecular nanoparticles belonging to such a class benefit from the pretargeted PET approach. ^{64}Cu-Tz probe was used as an imaging agent with TCO-modified supramolecular nanoparticles and showed preferential accumulation in tumors (Hou et al., 2016).

1.2   Radiochemistry

1.2.1   Fluorine-18 and its production

Fluorine-18 possesses a unique beneficial set of physical properties, placing it among the most frequently used positron-emitting radionuclides. In the first place, it has a reasonable half-life of 109.8 min, providing ample time for multi-step syntheses and transportation, but at the same time short enough not to cause unnecessary exposure. Secondly, it has a clean decay profile characterized by a 96.9% beta-decay. Finally, its maximum energy of 0.634 MeV is considered a low value. The above mentioned characteristics contribute to high resolution images using fluorine-18.

Fluorine-18 is produced with a cyclotron either in the form of [^{18}F]fluoride ions or [^{18}F]F$_2$ gas. The first one is more commonly used and derived from ^{18}O(p,n)^{18}F nuclear reaction using enriched [^{18}O]H$_2$O as the starting material. It comes from the aqueous target, making the handling and transfer easy and straightforward. It is produced as a no-carrier added aqueous solution, which ensures high molar activity, reported up to 5180 GBq/μmol (Solin et al., 1988).

Less popular but still of high value the fluorine-18 production method results in electrophilic [^{18}F]F$_2$ either from ^{20}Ne(d,α) ^{18}F or ^{18}O(p,n)^{18}F. The presence of

nonradioactive F_2 as a carrier makes handling the gaseous target more challenging and lowers the molar activity (Bergman & Solin, 1997).

1.2.2 ^{18}F-Fluorination

The approaches to introduce [^{18}F]fluorine into a molecule can be categorized into two main groups: direct and indirect radiolabeling. The direct method involves radiofluorination by directly introducing [^{18}F]fluoride into the precursor, but it is often associated with harsh reaction conditions, which can be challenging for sensitive biomolecules. In such cases, the indirect approach was found to be very useful, where fluorination occurs through the use of the fluorine-18 labeled building blocks. This method is not only beneficial in terms of mild reaction conditions but also allows the creation of a library of compounds. Once a synthesis method for fluorine-18 labeled building blocks is developed and introduced, it can be applied to other compounds.

1.2.2.1 Direct radiolabeling

Nucleophilic fluorination is a widely used method due to accessibility of the cyclotron-produced [^{18}F]fluoride and high molar activity achieved. For aliphatic positions, the typical reaction mechanism is S_N2 and for aromatic is S_NAr nucleophilic substitution, where fluoride acts as the nucleophile. However, solvated [^{18}F]F$^-$ is unreactive and needs activation, commonly achieved through the formation of the complex with polyethers kryptofix-2.2.2 or tetrabutylammoiumhydroxide (TBAOH), followed by azeotropic distillation using acetonitrile (ACN) (Figure 5) (Coenen, 2007).
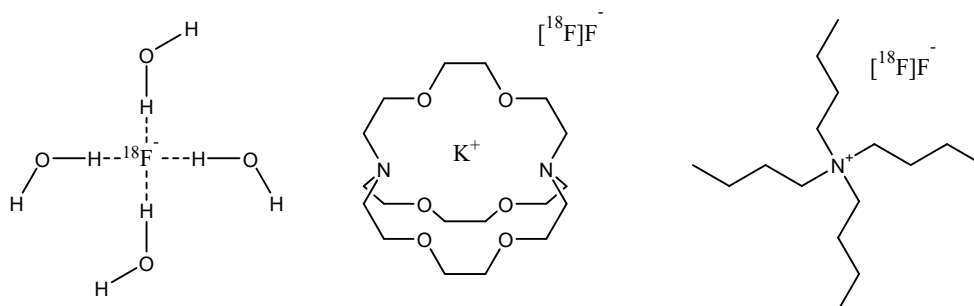
Figure 5. Innert solvated [^{18}F]F$^-$, K$^+$/K$_{2.2.2}$-complex of [^{18}F]F$^-$, and TBA[^{18}F]F$^-$.

The typical nucleophilic fluorination procedure starts with trapping [^{18}F]fluoride on an anion-exchange cartridge, followed by potassium carbonate and kryptofix-

2.2.2 elution. The eluted solution then undergoes the azeotropic distillation mentioned above, typically lasting around 20 minutes. Ongoing efforts are directed towards developing methods that eliminate the need for azeotropic distillation. One of them is solid phase extraction (SPE) (Orlovskaya et al., 2019).

The success of the nucleophilic substitution reaction also relies on carefully selected leaving groups. Among the most common leaving groups are triflate, tosylate, mesylate, and halides, with halides generally resulting in lower radiochemical yields (Deng et al., 2019; Jacobson et al., 2015).

In addition to S_N2 and S_NAr nucleophilic fluorination, another important approach includes transition metal-mediated ^{18}F-fluorination. Copper-mediated aromatic ^{18}F-fluorination allows simple and efficient late-stage fluorine-18 introduction utilizing haloarene, organoboron, iodonium, and C-H precursors (Wright et al., 2020).

Electrophilic radiolabeling approaches remain feasible, however, less popular, due to the addition of the F_2 gas as a carrier, leading to lower molar activities. It is highly reactive, however, it also results in more side products, complicating purification processes. Despite these limitations, electrophilic fluorination finds application in the production of 6-[^{18}F]fluoro-L-DOPA (Azad et al., 2007).

Post-target methods for generating electrophilic fluorination reagents have introduced new possibilities for the utilization of electrophilic fluorination. In such a method, [^{18}F]fluoride is utilized to produce [^{18}F]F_2 (Bergman & Solin, 1997; Krzyczmonik et al., 2017).

Currently, radical fluoromethylation attracted considerable attention as a radiolabeling approach, which allows avoiding pre-functionalization of the substrate. Trump et al. reported successful direct C−H ^{18}F-difluoromethylation of various N-heteroaromatics, xanthines, nucleic acid bases, and drug compounds with high molar activity and just with a two-minute photoredox reaction step (Trump et al., 2019).

1.2.2.2   Indirect radiolabeling

Most of direct radiofluorination methods are often unsuitable for introducing fluorine-18 into sensitive molecules due to the harsh reaction conditions. In such cases, the methods previously described for pretargeted PET become valuable as radiolabeling approaches, particularly due to the mild characteristic of click chemistry. Another practical option is the use of prosthetic groups.

Fluoroalkylation is used to introduce aliphatic building blocks, especially with small molecules, fluoroalkylation is a commonly employed method. The commonly used fluoroalkylation agents include [^{18}F]fluoromethyl bromide (Klein et al., 2015), [^{18}F]fluoroethyl tosylate (Beyerlein et al., 2013), and [^{18}F]fluoroethyl bromide (Schmaljohann et al., 2011).

Another interesting and valuable approach to radiolabel sensitive molecules is [18F]fluoroglycosylation. This method is chemoselective with high yields and can be conducted in aqueous solutions. [18F]fluoroglycosylation can also positively affect *in vivo* properties, like blood stability, bioavailability, and clearance of the tracer. However, usually an additional purification step is needed to remove the excess of the precursor (Shinde et al., 2021; Van Der Born et al., 2017).

Various methods can be used to create 18F-glucoconjugates, including oxime formation, click chemistry, and enzymatic reactions (Keinänen et al., 2016, 2018; X. G. Li et al., 2014; Maschauer et al., 2010; Shinde et al., 2021). While different glycosyl moieties are viable options, 2-[18F]fluoro-2-deoxy-*D*-glucose ([18F]FDG) stands as a golden standard and one of the most widely utilized tracers in PET imaging (Figure 6A) (Hamacher et al., 1986). Given its widespread availability, it is also reasonable to apply [18F]FDG as a prosthetic group for radiolabeling other PET tracers. For oxime-formation between [18F]FDG and amine to form glycosylamines, the glucose analog needs to be in an acyclic aldehyde form; this is achievable through mutarotation in an aqueous solution (Figure 6B). However, in aqueous environments, the equilibrium is predominantly shifted towards the cyclic form, making the acyclic aldehyde form less favorable and bringing the additional challenges for the oxyme formation. Nonetheless, the acyclic aldehyde form can be facilitated by acidic conditions and increased temperature.
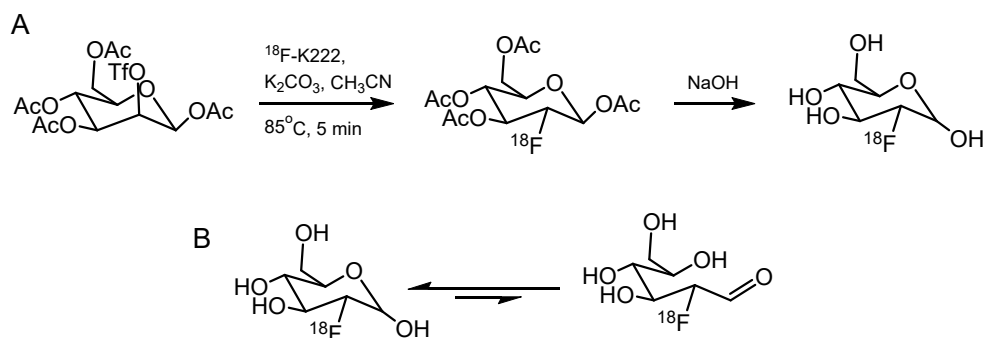
Figure 6. [18F]FDG synthesis (A); [18F]FDG mutarotation: cyclic and aldehyde forms (B).

Oxime bond formation is an excellent choice in [18F]fluoroglycosylation due to its high biocompatibility, selectivity, and efficiency, making it suitable for aminooxy-functionalized peptide radiolabeling (Hultsch et al., 2009; Namavari et al., 2009; Şenk et al., 2018; Wuest et al., 2009). Radiolabeled with this method peptides were reported with high radiochemical yield (RCY) and great purity. The folate moiety, as a valuable targeting vector, also found application in [18F]fluoroglycosylation, revealing promising tumor uptakes in *in vitro* and *in vivo*

studies (Al Jammaz et al., 2012; Fischer et al., 2012, 2013). The indirect radiofluorination is also applicable for glycosylated tetrazine derivatives production utilizing both [^{18}F]FDG (Keinänen et al., 2018; Rashidian et al., 2015; Simeonova et al., 2023) and [^{18}F]FDR (Keinänen et al., 2016). In this study, amino-oxy-derived phenyltetrazine was radiolabeled with [^{18}F]FDG via oximation to use radiolabeled tetrazine for the IEDDA reaction (Äärelä et al., 2023; Auchynnikava et al., 2023).

As mentioned earlier, click chemistry offers versatile techniques when synthesizing PET tracers in a targeted imaging approach. Click chemistry has broadened the possibilities for radiolabeling sensitive substrates, offering mild reaction conditions, and quick reaction rates, critical and desirable in radiochemistry. While CuAAC is not easily applicable for *in vivo* radiolabeling due to toxicity, it is widely used in [^{18}F]fluoroglycosylation to create imaging agents (Arja et al., 2018; Banerjee et al., 2013; Hugenberg et al., 2012).

For the successful incorporation of the [^{18}F]FDG during [^{18}F]fluoroglycosylation the removal of the precursor is essential, often requiring a semi-preparative high-performance liquid chromatography (HPLC) step to avoid competition from the unlabeled carbohydrate precursor in further reaction steps. It means that the commercially available [^{18}F]FDG should undergo purification before further usage.

1.2.2.3 ^{18}F-Labeling through B-, Si-, Al-, S-^{18}F bond formations

Over the past decades, B-, Si-, Al-, S-^{18}F bond formation has been utilized for ^{18}F-labeling. This type of labeling is applicable for biomolecules due to the efficiency of the process in an aqueous solution, which is based on high bond dissociation energies (Rong et al., 2023).

Silicon-fluoride acceptor (SiFA) radiolabeling offers rapid fluorination via ^{19}F/^{18}F isotopic exchange. SiFA radiolabeling is suitable for peptide and protein production and has recently led to clinical studies of [^{18}F]-SiFA*lin*-TATE in patients with neuroendocrine tumors (Ilhan et al., 2019). The introduction of alkylammniomethyltrifluoroborate (AmBF$_3$) by Liu et al. (Z. Liu et al., 2015) has enabled its use in radiolabeling a variety of water-soluble biomolecules for preclinical (Otaru et al., 2022) and clinical (Chausse et al., 2022) studies. Sulfur (VI) fluoride exchange (SuFEx) has also been reported to provide fast late-state ^{18}F-fluorination and has been successfully applied to produce a library of aryl fluorosulfates under mild conditions (Zheng et al., 2021). As fluorine can form strong bonds with aluminum Al^{3+}, another feasible method is creating [^{18}F]F-Al complex, which then could be incorporated into a chelate, such as NOTA (McBride et al., 2010, 2013). While this approach has been shown to be quick and simple when radiolabeling small molecules and peptides, it is inferior in terms of molar activities and the ability of the chelate to influence biodistribution.

The introduction of the prosthetic group may affect the biodistribution of the final molecule. The smaller the compound, the greater will be the prosthetic group influence. However, it is not always a disadvantage, as careful consideration of the potential effects allows us to control them to our advantage. For instance, in aluminum with chelate we can increase the hydrophilicity of the compound, or in the case of lipophilic protein aluminum [^{18}F]fluoride radiolabeling will improve its biodistribution.

1.3 Molecular spherical nucleic acids

Spherical nucleic acids (SNAs) represent highly oriented nucleic-based nanostructures. Their distinctive spherical morphology originates from a dense shell of radially oriented ONs attached to the surface of a nanoparticle core. Various materials could be used for the core, e.g. gold, silver, quantum dots, platinum, fullerene, micelles, or liposomes (Figure 7). The radially oriented ONs typically consist of DNA or RNA sequences, playing the role of the targeting moiety. Due to its highly oriented structure and despite differences in building blocks, SNAs share common advantages over their linear counterparts. These advantages include the resistance to nuclease degradation, muted innate immune responses, enhanced cellular uptake, and avoidance of the renal clearance. The above mentioned beneficial properties position SNAs as great deliver agents and promising tools for studying biological processes (Mirkin et al., 1996; Mokhtarzadeh et al., 2019). The challenge associated with SNA, as well as with numerous other drug delivery platforms, lies in a structural polydispersity. The development of SNAs with well-defined structures is essential for the development and detailed characterization of delivering agents. Molecular spherical nucleic acids (MSNAs) with fullerene core have lower ON capacity, but were synthesized with molecularly defined structures (Gulumkar et al., 2021; H. Li et al., 2018) and are in question in this study.

It is important to characterize the properties and biodistribution profile of novel therapeutic molecules, to understand the possible *in vivo* interaction, clearance route, and to validate targeting characteristics. Imaging methods play a particularly valuable role in this task. For SNA, extensive studies have been conducted using a variety of microscopy methods (Bousmail et al., 2017; Kyriazi et al., 2022; H. Li et al., 2018; M. Liu et al., 2021).
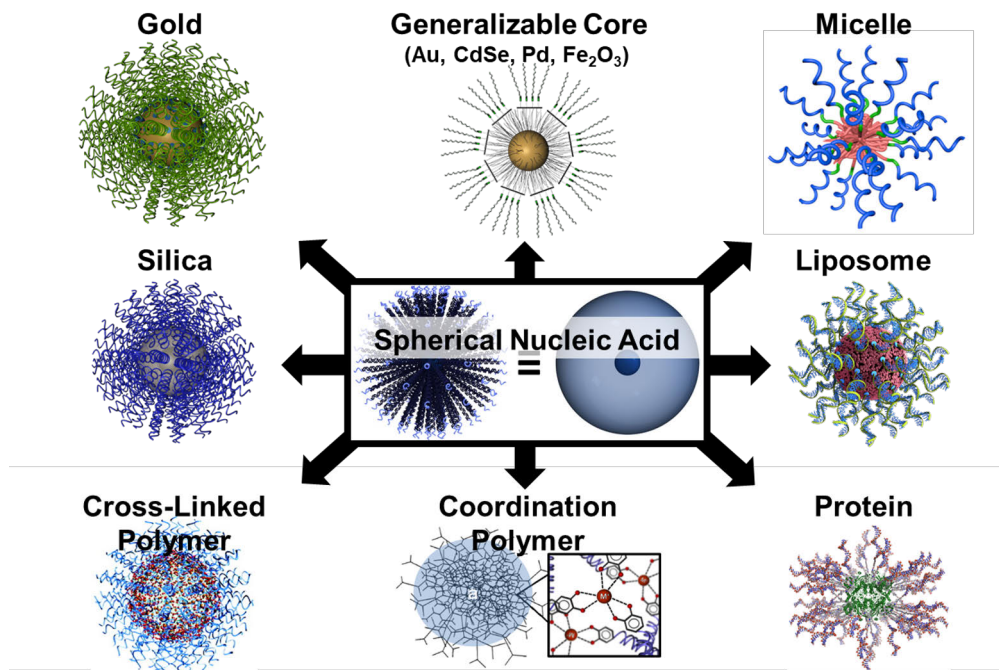
Figure 7. A variety of SNA structures. Reprinted with permission from https://mirkin-group.northwestern.edu/project/spherical-nucleic-acids/.

Among imaging methods, PET is essential as it helps when visualizing and quantifying SNA biodistribution *in vivo,* providing dynamic information without interference from the amount of drug tracer administered. It provides molecular-level information. The development of MSNA as a potential delivery vehicle necessitates a thorough investigation of the particularly engineered SNA biodistribution. Understanding possible accumulation sites or elimination routes is critical. The development of monofunctionalized method for radiolabeling well-defined MSNA facilitated the biodistribution monitoring (Gulumkar et al., 2021). For this purpose the direct radiolabeling utilizing click chemistry is essential due to its mild conditions and rapid reactions. However, as a nanomaterial, some MSNA structures may exhibit long circulation times. Investigating them with PET might require long-lived radionuclides, bringing the challenge of increased radiation exposure for the patient. In such cases, the pretargeted approach becomes valuable and can be utilized with common short-lived radionuclides.

2 Aims

The aim of this work was to develop radiolabeling methods for targeted and pretargeted PET imaging in order to explore the structural effects of MSNAs. To achieve this, six different MSNA structures were directly radiolabeled with [^{18}F]FDG-Tz and compared with single-stranded ON and [^{18}F]FDG-Tz biodistribution; in addition to which MSNA was evaluated using a pretargeted approach.

Specific aims were:

- To synthesize and biologically evaluate [^{18}F]FDG-Tz in healthy mice as a potential candidate for pretargeted PET imaging.

- To utilize [^{18}F]FDG-Tz for direct radiolabeling of a variety of MSNA structures to detect and quantify the impact of backbone chemistry, folate decoration, and TCO-load percentage on MSNA biological behavior in HCC1954 tumor-bearing mice.

- To investigate MSNA by using the pretargeted approach by using [^{18}F]FDG-Tz.

3   Materials and Methods

3.1   General

Unless otherwise stated, all the reagents were purchased from commercial providers and used without any additional purification. Ultrapure water (> 18.2 MΩ cm^{-1}) was used for all experiments. More detailed information regarding the providers, reagents, instruments, materials, and methods are described thoroughly in original publications (I-III).

^{1}H- and ^{13}C- nuclear magnetic resonance (NMR), performed with Bruker 500 MHz spectrometer, was performed to confirm the correct structures of the synthesized reference compounds (FDG-Tz and FDR-Tz). Chemical shifts are reported in parts per million (ppm).

[^{18}F$^-$]Fluoride for radiosyntheses in Studies I-III was produced in-house from ^{18}O-enriched water (Rotem Industries Limited, Arava, Israel) using CC 18/9 cyclotron (Efremov Institute of Electrophysical Apparatuses, St. Petersburg, Russia). The syntheses were conducted in a semi-automated device (DM Automation, Nykvarn, Sweden), and the flow chart of the device is presented in Figure 8. RCY was calculated from decay-corrected to the end of bombardment (EOB) activity of the end product and initial activity at EOB.
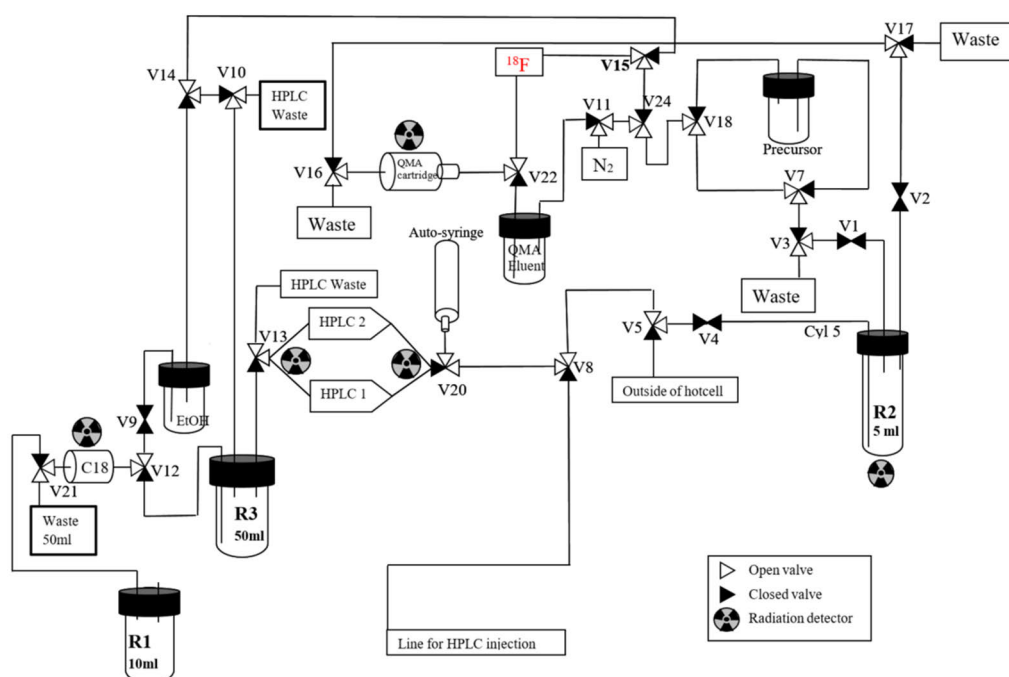
Figure 8. Flow chart of the semi-automated device for synthesis of the radiopharmaceuticals.

The purity of the synthesized radiopharmaceuticals and reference compound was assessed using radio-thin-layer chromatography (TLC) and radio-HPLC or radio-size-exclusion chromatography (SEC). Semi-preparative HPLC was used for purification during the intermediate and final steps of the [^{18}F]FDG-Tz production. The specific conditions for HPLC methods are listed in Table 3.

To prepare tumor-bearing mice HCC1954 ductal breast carcinoma cells were obtained from American Type Culture Collection (ATCC, Manassas, VA, USA). The cells were cultured in a media containing 10% FBS (fetal bovine serum) and 0.5% penicillin-streptomycin at +37°C in the presence of 5% CO_2.

Table 3. Semi-preparative and analytical HPLC methods.

Study	Compound	Column	Method	Flow (ml/min)
I, II, III	[18F]FDG (semi-preparative)	Germini, 5 µm, 110Å, 250 mm × 10 mm	A: H_2O B: ACN 0-20 min 22-56% B 20-42 min 56-85% B	4
I, II, III	[18F]FDG-Tz (semi-preparative)	Jupiter Proteo, 4 µm, 90Å, 250 mm × 10 mm	A: 0.1% TFA* B: 0.1% TFA in ACN 0-15 min 12-22% B 15-20 min 22% B	4
I, II, III I	[18F]FDG-Tz (analytical) FDG-Tz	Jupiter Proteo, 4 µm, 90Å, 250 mm × 4.6 mm	A: 0.1% TFA B: 0.1% TFA in ACN 0-15 min 15-35% B 15-20 min 35% B	1
I, II, III	[18F]MSNA-PO [18F]MSNA-PS [18F]ON [18F]Fol-MSNA-PO [18F]Fol-MSNA-PS [18F]TCO(140%)-MSNA [18F]TCO(400%)-MSNA	Waters Protein-Pak 33SW, 7.5 × 300 mm	0.1 M KH_2PO_4, pH 7.0	1

* TFA – trifluoroacetic acid.

3.2 [18F]FDG-Tz

3.2.1 Synthesis of the reference compounds

N-(4-(1,2,4,5-tetrazin-3-yl)benzyl)-2-((((2S,3S,4R)-2-fluoro-3,4,5,6-tetrahydroxyhexylidene)amino)oxy)acetamide (FDG-Tz)

FDG-Tz was synthesized according to (Keinänen et al., 2018). N-(4-(1,2,4,5-tetrazin-3-yl)benzyl)-2-(aminooxy)acetamide hydrochloride (14.0 mg, 47.3 µmol) was dissolved in 1.5 ml water. FDG (77.6 mg, 426 µmol, 9 eq) was added to a tetrazine aqueous solution and kept for 3 h at room temperature (r.t.). The resulting mixture was purified by passing it through AminoLink resin, which was then washed with 2 ml of water. Subsequently, the mixture was applied to C18 Sep-Pak cartridge (preconditioned with 5 ml of ethanol and 10 ml of water), which was washed with an additional 10 ml of water. ACN (5 ml) was used to elute the product, which was then evaporated to dryness. The FDG-Tz synthesis scheme is presented in Figure 9.

^{1}H NMR (500.08 MHz, DMSO) δ 10.57 (s, 1H), 8.53 (dt, J = 7.6 Hz, 1H), 8.46 (d, J = 8.4 Hz, 2H), 7.76 (t, J = 7.2 Hz, 1H), 7.55 (m, 3H), 7.17 (q, J = 5.3 Hz, 0.20H), 5.76 (dt, J = 12.4 Hz, 0.18H), 5.52 (d, J = 5.4 Hz, 0.23H), 5.24 (d, J = 6.7 Hz, 1H), 5.20 (d, J = 5.6 Hz, 1H), 5.14 (d, J = 6.7 Hz, 0.75H), 5.04 (dt, J = 12.4 Hz, 0.18H), 4.86 (d, J = 8.3 Hz, 0.17H), 4.61-4.57 (m, 4H), 4.49-4.45 (m, 2H), 4.43-4.39 (m, 1H), 4.17 (d, J = 9.1 Hz, 0.36H), 4.03-3.96 (m, 1H), 3.71-3.68 (m, 0.48H), 3.61-3.57 (m, 1H), 3.52-3.48 (m, 2H). ^{13}C-NMR (125.75 MHz, DMSO-d6) δ: 170.49, 169.21, 165.90, 158.56, 149.38, 149.20, 145.10, 130.80, 128.45, 128.23, 91.87, 90.51, 78.67, 73.11, 71.44, 70.38, 70.21, 70.09, 70.06, 63.68, 61.32, 42.02.
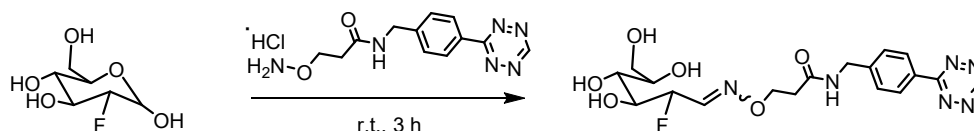
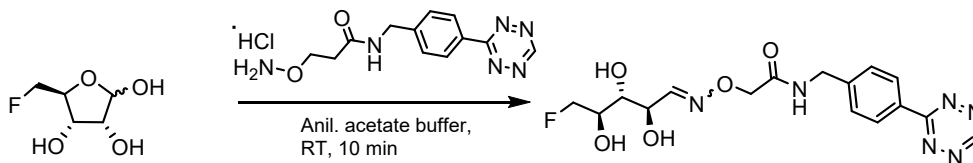**Figure 9.** FDG-Tz synthesis scheme.

N-(4-(1,2,4,5-tetrazin-3-yl)benzyl)-2-((((2R,3R,4R)-5-fluoro-2,3,4-trihydroxypentylidene)amino)oxy)acetamide) (FDR-Tz)

FDR-Tz was synthesized according to (Keinänen et al., 2016). N-(4-(1,2,4,5-tetrazin-3-yl)benzyl)-2-(aminooxy)acetamide hydrochloride (7.2 mg, 24.3 µmol, 1eq.) was dissolved in 1.25 ml of anilinium acetate buffer (1.2M, pH 4.6) and 3.5 ml of water. FDR (14.4 mg, 94.9 µmol, 3.9 eq.) was added, and the reaction mixture was left for 10 minutes at r.t. Subsequently, the reaction mixture was passed through two C18 Sep-Pak cartridges (preconditioned with 5 ml of ethanol and 10 ml of water). The cartridges were sequentially washed with 40 ml of water, 40 ml of 1% ethanol, and 10 ml of 2.5% ethanol. The cartridges were eluted with 40 ml of 5% ethanol and 30 ml of 10% ethanol, 1.5 ml fractions were collected. Product fractions, identified by their pink color and TLC, were combined and evaporated to dryness. FDR-Tz synthesis scheme is presented in Figure 10.

^{1}H NMR (500 MHz, acetone) δ = 10.44 (s, 1H), 8.54 (d, J = 8.2 Hz, 2H), 8.12 (br, 0.19H), 7.83 (br, 0.88H), 7.65 (d, J = 7.0 Hz, 0.85H), 7.62 (d, J = 8.6 Hz, 2H), 6.96 (d, J = 6.5 Hz, 2H), 5.19 (q, J = 3.6 Hz, 0.21H), 4.78 (d, J = 5.9 Hz, 0.10H), 4.67-4.55 (m, 5H), 4.55 (s, 1H), 4.50-4.47 (m, 2H), 4.38 (d, J = 5.1 Hz, 0.37H), 3.92-3.85 (m, 1H), 3.78-3.76 (m, 1H). ^{13}C-NMR (125.75 MHz, acetone) δ: 169.39, 166.21, 158.15, 153.47, 152.87, 144.92, 130.87, 128.26, 128.20, 127.99, 85.67, 84.34, 72.95, 72.90, 72.64, 71.12, 70.98, 70.32, 41.87.

Figure 10. FDR-Tz synthesis scheme.

3.2.2   [^{18}F]FDG-Tz radiosynthesis

[^{18}F]FDG-Tz was synthesized via a two-step protocol, with detailed steps outlined in Figure 11. [^{18}F$^-$]fluoride was loaded to a quaternary methyl ammonium (QMA) Plus Light Sep-Pak cartridge (preconditioned with 10 ml of 0.5 M K$_2$CO$_3$, 15 ml of water). The cartridge was eluted with a solution containing Kryptofix 2.2.2, K$_2$CO$_3$, Milli-Q water, and ACN as K$^+$/K$_{2.2.2}$-complex of [^{18}F]F$^-$. The solution was azeotropically dried with anhydrous ACN at 120°C for an average of 15-20 minutes under Ar flow. After visible inspection of the moisture absence in the reaction vessel and outflowing line, the reaction vessel was cooled down to 50°C. 1,3,4,6-tetra-O-acetyl-2-O-trifluoromethanesulfonyl-β-*D*-mannopyranose (25 mg, 52 μmol) in ACN (0.5 ml) and thexyl alcohol (0.1 ml) were added to the reaction mixture, and heated at 85°C for 5 min. After cooling down to 50°C and diluted with 0.8 ml of water the reaction mixture was injected into a semi-preparative HPLC. All semi-preparative and analytical HPLC methods and conditions are presented in Table 3. The isolated fraction was collected into a bottle with 30 ml water and loaded into a tC18 Plus Light cartridge (preconditioned with 10 ml of ethanol and 10 ml of water). To deprotect and elute 2 M NaOH (0.2 ml) was passed through the cartridge into the receiving vial with 25 μl of 6 M HCl. As a second step N-(4-(1,2,4,5-tetrazin-3-yl)benzyl)-2-(aminooxy)acetamide hydrochloride (0.57 mg, 1.9 μmol in 37.5 μl of water), 40 μl of methanol, and 80 μl of anilinium acetate buffer (1.2 M, pH 4.6) were added to obtained glucose-free [^{18}F]FDG. The reaction mixture was kept at 75°C for 30 min. The mixture was diluted with water for semi-preparative HPLC. The collected fraction was diluted with 25 ml of water and loaded into two C18 Plus Light cartridges (preconditioned with 5 ml of ethanol and 10 ml of water). [^{18}F]FDG-Tz was eluted with 0.5 ml of absolute ethanol and evaporated at 80°C for 5 min. The final product was formulated in phosphate-buffered saline (PBS).
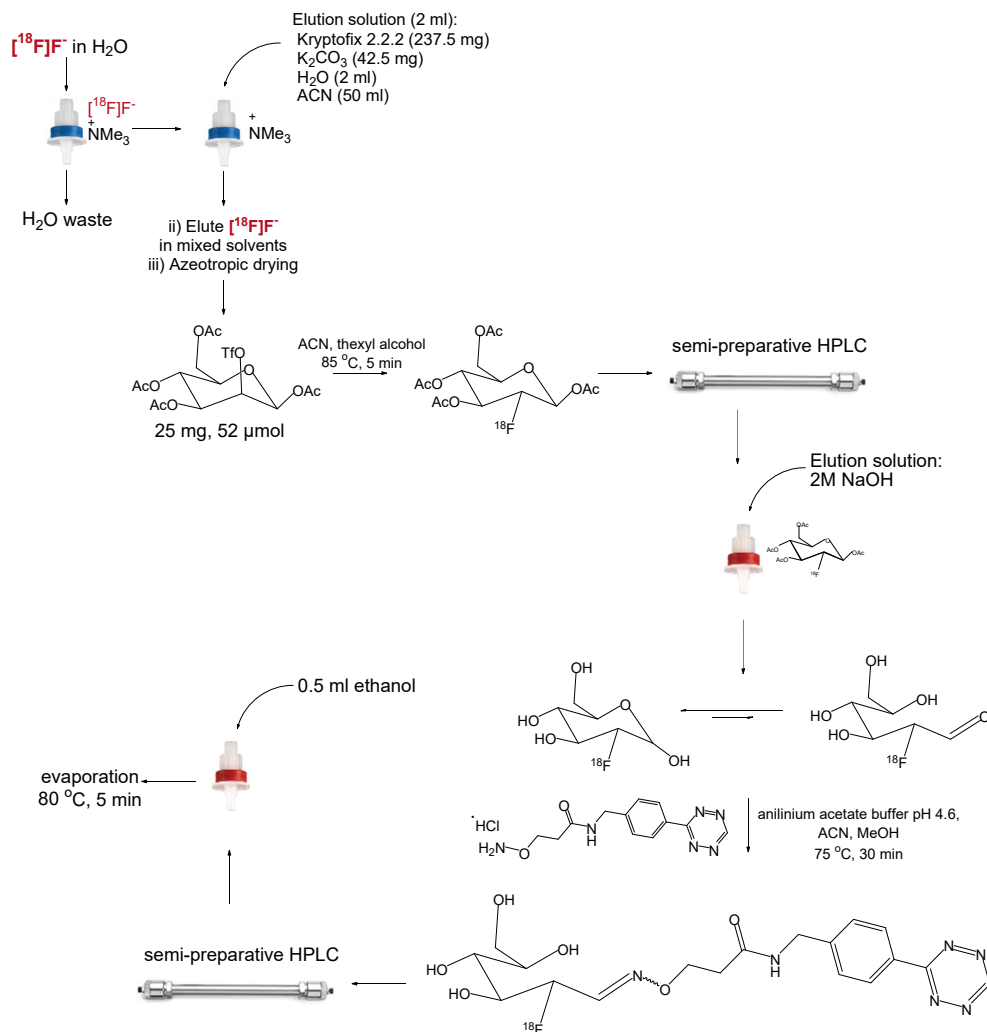
Figure 11. Schematical representation of the [18F]FDG-Tz radiosynthesis.

3.3 GLUT1 binding affinity and cellular uptake

GLUT1 (glucose transporter 1) binding affinity and cellular uptake of FDR-Tz and FDG-Tz was conducted by Prof. Jarkko Rautio's group at the School of Pharmacy, University of Eastern Finland. The detailed process is described in Study I. Briefly, cultured CAL27 squamous cell carcinoma cells were utilized to evaluate the ability of FDR-Tz and FDG-Tz to compete for GLUT1-binding with a known radiolabeled GLUT1 substrate, D-[14C]-glucose. The liquid scintillation counter was used to measure the radioactivity. The half-maximal inhibitory concentration (IC_{50}) was determined through nonlinear regression analysis. Concentration-dependent cell

uptake of FDR-Tz and FDG-Tz was investigated in CAL27 cells, followed by liquid chromatography-tandem mass spectrometry (LC-MS/MS) analysis to quantify the compounds in cell lysates.

3.4   MSNAs and single-stranded ON

3.4.1   Syntheses of MSNAs and single-stranded ON

MSNAs and single-stranded ON were provided by Prof. Pasi Virta's group from the Department of Chemistry, University of Turku. Briefly, ONs were synthesized from commercially available 2′-deoxyribonucleotide building blocks using an automated DNA/RNA synthesizer. For the sulfurization of some ONs, 3-phenyl 1,2,4-dithiazoline-5-one (POS) was used. As a first step, bicyclononyne (BCN)-modified HER2 messenger RNA (mRNA) targeting antisense ON was attached to a C_{60} core. Then the obtained C_{60}-ON conjugate was mixed with BCN–ON to attach the rest of the ONs arms, and produce [NH_2]MSNA with either phosphodiester (PO) or phosphorothioate (PS) backbones. TCO-modified MSNAs were obtained by mixing TCO-PEG$_4$-NHS ester with [NH_2]MSNA. To make folate-modified MSNAs folate N-hydroxysuccinimidyl ester was applied to ONs and TCO-modified MSNAs were treated with obtained Fol-ONs. The authenticity and homogeneity of the final products were confirmed by SEC equipped with a multiple angle light scattering detector (SEC-MALS) and by polyacryl amide gel electrophoresis (PAGE).

Single-stranded ON was synthesized as well by using an automated DNA/RNA synthesizer with the following TCO-functionalization using TCO-PEG$_4$-NHS. The final product was purified with HPLC and authenticated with mass spectrometry.

TCO-monofunctionalized MSNAs, e.g. MSNA-PO, MSNA-PS, Fol-MSNA-PO, and Fol-MSNA-PS, have a 25% TCO-load, meaning one out of every fourth MSNA in the heterogenic mixture has a TCO attached. The two other MSNA compounds with PS backbones, TCO(140%)-MSNA and TCO(400%)-MSNA, have an 140% and 400% TCO-load, respectively.

3.4.2   Radiolabeling of MSNAs and single-stranded ON

To radiolabel TCO-modified MSNAs and single-stranded ON, part of the [^{18}F]FDG-Tz tracer diluted with PBS was mixed with TCO(140%)-MSNA and TCO(400%)-MSNA for Study I, with a MSNA-PO, MSNA-PS, single-stranded ON for Study II and a Fol-MSNA-PO and Fol-MSNA-PS for Study III. In all the reactions, the ratio between tetrazine and TCO was maintained between 1:2 and 1:4. After 5 minutes at r.t. the reaction mixture was subjected to ultrafiltration (14100 × g for 3×5 min), and

0.01M RNase-free PBS (pH 7.4) was used for the formulation of the final product. The radiolabeled structures are presented in Figure 12.
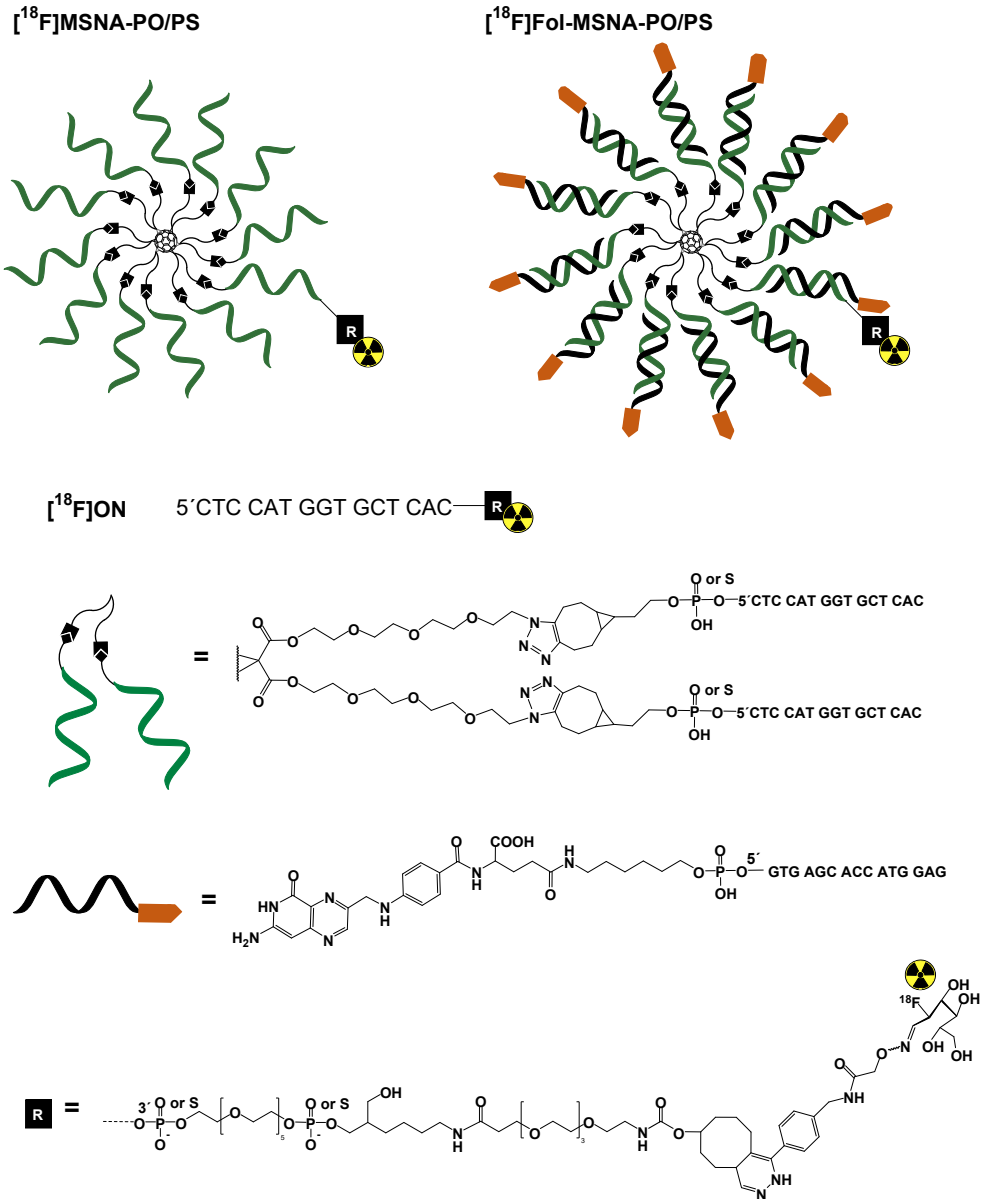
Figure 12. Radiolabeled MSNAs ([18F]MSNA-PO, [18F]MSNA-PS, [18F]Fol-MSNA-PO, [18F]Fol-MSNA-PS) and single-stranded ON ([18F]ON) structures.

3.5 Biological evaluation

All animal experiments were approved by the national Project Authorization Board in Finland (licenses: ESAVI/12132/04.10.07/2017 and ESAVI/8648/2020) and carried out in compliance with the European Union Directive 2010/EU/63 on the protection of animals used for scientific purposes.

Mice had access to standard soy-free food and tap water *ad libitum* except in Study I which investigated the effect of fasting on the biodistribution of [^{18}F]FDG-Tz. In this case, the animals were required to have fasted for 4 h prior to the tracer injection. For subcutaneous cell inoculation, imaging, and sacrifice animals were anesthetized with isoflurane.

3.5.1 Animal models

In Study I, [^{18}F]FDG-Tz was first evaluated in healthy female Balb/cAnNrj mice. To evaluate different MSNA structures and test pretargeted approach (Studies I-III) Rj:Athymic-*FOXN1$^{nu/nu}$* female mice were inoculated with HCC1954 ductal breast carcinoma cells. Comprehensive details regarding the animal models, the ages, and number of animals used in Studies I-III are listed in Table 4.

Most of the tumors were developed with fluid-filled, necrotic cores, which were visual in PET/CT images, *ex vivo* autoradiography, and hematoxylin and eosin (H&E) staining. The image analysis was done accordingly excluding the core. Details are given in the supplemental information for Study I.

Table 4. Animal models, age, and amounts used.

Study	Radiopharmaceutical	Animal model	Age	Animals amount
I	[^{18}F]FDG-Tz	healthy female Balb/cAnNrj mice	9-14 weeks 19 weeks (fasting studies)	21
I	[^{18}F]TCO(140%)-MSNA [^{18}F]TCO(400%)-MSNA Pretargeted			16
II	[^{18}F]FDG-Tz [^{18}F]MSNA-PO [^{18}F]MSNA-PS [^{18}F]ON	Rj:Athymic-*FOXN1$^{nu/nu}$* female mice bearing subcutaneous HER2-expressing HCC1954 tumors	8-10 weeks	24
III	[^{18}F]Fol-MSNA-PO [^{18}F]Fol-MSNA-PS			16

3.5.2 *In vivo* PET/CT imaging, image analysis and *ex vivo* biodistribution

For all *in vivo* studies mice were first imaged with CT for anatomical reference, followed by an intravenous tracer injection via the tail vein, and an immediate dynamic 60-minute PET scan. Imaging of [^{18}F]FDG-Tz in healthy mice (Study I) was conducted using Molecubes β-cube (PET) and X-cube (CT) with time frames 30×10 s, 15×60 s, 4×300 s, 2×600 s, while all other tracer evaluations in tumor-bearing animals were imaged with Inveon Multimodality PET/CT (time frames 6×10 s, 4×60 s, 11×300 s).

PET data were quantified by defining regions of interest (ROIs) and presenting results as time-activity curves (TACs) with standardized uptake values (SUVs). Image analysis was performed with in-house developed Carimas software (v2.10, Turku PET Centre, Turku, Finland), and the presented images were prepared with an Inveon workspace.

Following imaging, the animals were euthanized under deep anesthesia by cardiac puncture and cervical dislocation. Organs of interest were harvested, weighed, and measured for radiotracer uptake using a Triathler 3″ gamma counter (Hidex, Turku, Finland). Results for the organs of interest were converted into injected dose per gram of tissue (%ID/g). Tumors were collected for further cryosectioning, autoradiography, H&E staining (3.5.4 Autoradiography and H&E staining) or *in vitro* binding studies (3.5.5 *In vitro* binding and blocking).

3.5.3 Pretargeted approach

For the pretargeted experiment, animals were first intravenously injected with TCO-MSNA (2.5 nmol of TCO in 50 µl), followed by the administration of an [^{18}F]FDG-Tz (5.4 ± 0.2 MBq in 40-80 µl, 52.7-118 pmol) injection twenty minutes after the TCO-MSNA injection. The dynamic PET imaging started simultaneously with the tracer injection (Figure 13). After imaging, the animals were sacrificed for *ex vivo* evaluation as described in 3.5.2.
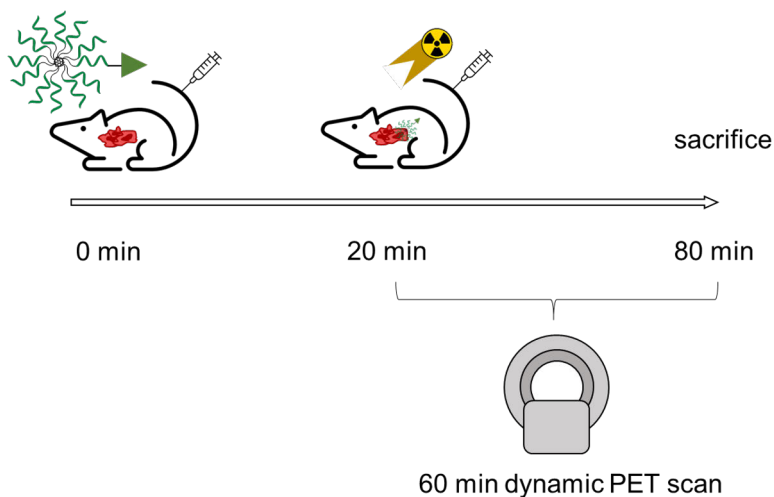
Figure 13. Pretargeted imaging approach by using [^{18}F]FDG-Tz and TCO(140%)-MSNA.

3.5.4   Autoradiography and H&E staining

The collected frozen tumors were cryosectioned into 20 μm slices for autoradiography and placed on the microscope slides. These tumor sections were then exposed to phosphor imaging plates for approximately 4 h (at least 2 half-lives) before scanning with a Fujifilm BAS-5000 scanner. Subsequently, the same slides underwent H&E staining.

3.5.5   *In vitro* binding and blocking

In Study III, *in vitro* binding and blocking studies were performed to prove the ability of the folate moiety of MSNA structures to bind to folate receptors (FRs). Tumor sections were treated with Al[^{18}F]F-1,4,7-triazacylononane-1,4,7-triacetic acid-conjugated folate ([^{18}F]-FOL), a compound known to bind to FRs (Silvola et al., 2018), provided by Anne Roivainen's group. A number of the slides were pre-treated with unlabeled Fol-MSNA-PO. The slides were then exposed and scanned in the same manner as the autoradiography (3.5.4 Autoradiography and H&E staining).

4 Results

4.1 Radiopharmaceutical synthesis and characterization

4.1.1 [^{18}F]FDG-Tz

[^{18}F]FDG-Tz was produced with 7% RCY. It yielded 191.5 ± 89.0 and 861.5 ± 462.3 MBq at the end of synthesis (EOS) depending on the starting activity, 8 GBq and 40 GBq, respectively, with a total synthesis time of 3.5 h. In the case of the [^{18}F]FDG-Tz evaluation, the purity of the end product was >95% according to radio-HPLC and radio-TLC (Figure 14). [^{18}F]FDG-Tz stability was tested up to 6 h, with 95% radiochemical purity (RCP) still remaining at 6 h. For [^{18}F]FDG-Tz produced for further MSNA radiolabeling, RCP was >91%, but was, however, not always tested, instead [^{18}F]FDG-Tz was directly used for the MSNA labeling followed by purification of the radiolabeled MSNA. Radiochemical properties of the produced [^{18}F]FDG-Tz are described in Table 5.

Table 5. Properties of [^{18}F]FDG-Tz.

	[^{18}F]FDG-Tz	[^{18}F]FDG-Tz for MSNA radiolabeling
Starting radioactivity, GBq	8	40
Activity EOS, MBq	191.5 ± 89.0	861.5 ± 462.3
Radiochemical yield (decay corrected), %	$7.0\% \pm 3.4$	$6.6\% \pm 3.5$
Radiochemical purity, %	>95%	>91%
Molar activity, GBq/µmol	14.7 ± 4.0	111.7 ± 37.2
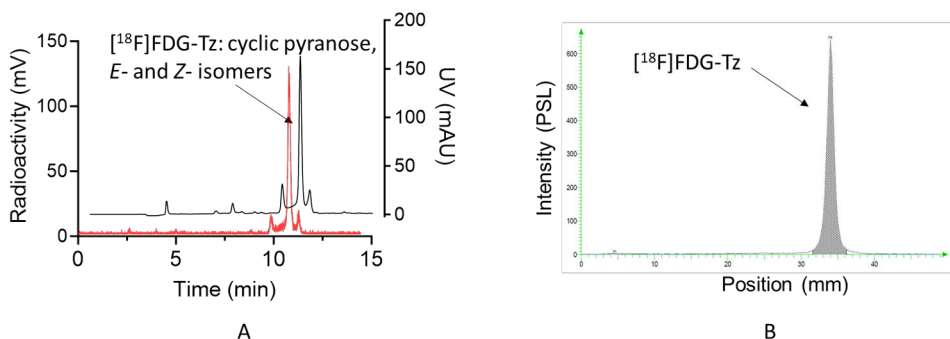
Figure 14. [¹⁸F]FDG-Tz end-product quality control: radio-HPLC (A); radio-TLC (B). Modified and reprinted with permission (Auchynnikava et al., 2023).

4.1.2 Radiolabeling of MSNAs and single-stranded ON

The MSNA structures and single-stranded ON radiolabeling was carried out over the course of 4 hours, including [¹⁸F]FDG-Tz production. The IEDDA radiochemical conversion, determined by radio-TLC of the crude product, was highly dependent on the tetrazine to TCO ratio and ranged from 54.5% to 100%, with an average of 91.4% ± 15.4 after a 5-minute reaction. Longer reaction times were also investigated without further IEDDA yield improvement. RCP for all radiolabeled MSNA structures was >99%.

4.2 Biological evaluation of [¹⁸F]FDG-Tz

4.2.1 GLUT1 binding and cellular uptake

To compare GLUT1 binding and cellular uptake of FDG-Tz and FDR-Tz studies in CAL27 cells were conducted. IC_{50}, determined in CAL27 cells, was 324.4 µM for FDG-Tz and 22.4 µM for FDR-Tz. The Michaelis-Menten kinetic parameters, the maximum rate of the reaction, when GLUT1 is saturated with substrate V_{max} and the substrate concentration at ½ V_{max} are presented in Table 6.

Table 6. GLUT1 binding and cellular uptake results in CAL27 cells.

	FDG-Tz	FDR-Tz
IC_{50}, µM	324.4	22.4
V_{MAX}, pmol/min/mg of protein	63.2 ± 8.5	27.8±3.7
K_m, µM	27.6 ± 13.8	3.6 ± 7.8

4.2.2   *In vivo* PET imaging

Dynamic PET imaging in healthy mice demonstrated the favorable pharmacokinetics of [^{18}F]FDG-Tz as a potential pretargeted agent (Figure 15). Radioactivity quickly eliminated from blood (SUV 0.43 ± 0.06 at 60 min) primarily through urinary excretion. Moderate residual uptake was observed in the liver at 60 minutes post-injection, with SUV of 2.00 ± 0.57.
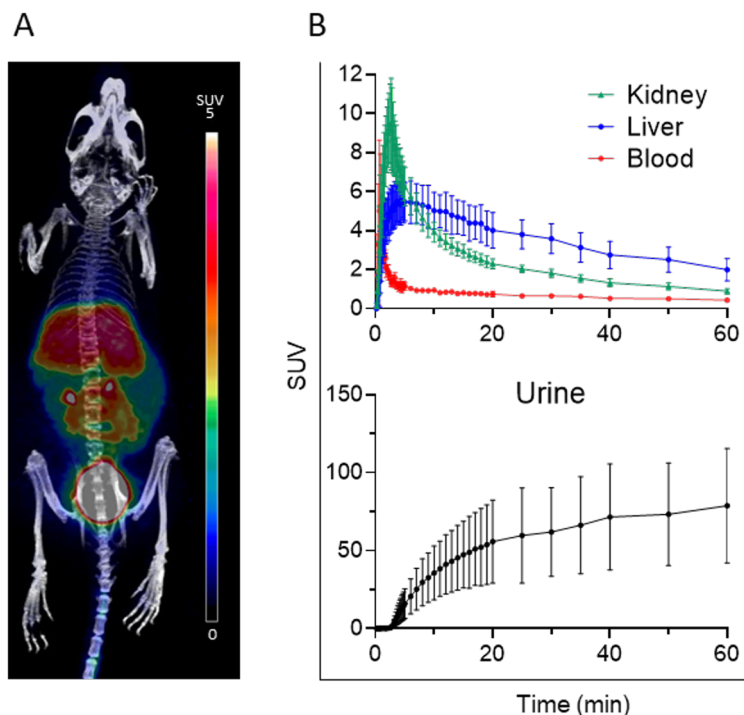
Figure 15. Biological evaluation of [^{18}F]FDG-Tz in healthy mice: maximum intensity projection PET/CT image (A); SUV time-activity curves for blood, liver, kidney, and urine (B). Reprinted with permission (Auchynnikava et al., 2023).

4.2.3   *Ex vivo* evaluation

Radioactivity distribution in the blood components (Figure 16A) demonstrated an increase in blood cell binding from 38% to 58% and in the plasma protein binding from 9% to 23% between 15 and 60 minutes post-injection.

  Ex vivo results, presented as %ID/g of excised tissues at 15, 30, and 60 minutes (Figure 16B), were consistent with PET image data, confirming quick blood elimination and urinary excretion. In addition, *ex vivo* revealed signs of minor hepatobiliary elimination of [^{18}F]FDG-Tz, with moderate gallbladder radioactivity

at 60 minutes (7.0 ± 0.7 %ID/g). Both the *in vivo* PET image (Figure 15A) and the *ex vivo* biodistribution (Figure 16B) showed low abdominal uptake (in the stomach, small and large intestines). Importantly, low tibia bone uptake (0.26 ± 0.04 at 60 minutes post-injection) indicates the absence of defluorination.

The low uptake of [^{18}F]FDG-Tz in GLUT1-rich tissues, together with the fasting studies, showed no significant difference between fasted and non-fasted animals at 15 minutes post-injection with a notable variation in gallbladder and urine uptake (Figure 16C), indicating the absence of GLUT1 transportation *in vivo*.
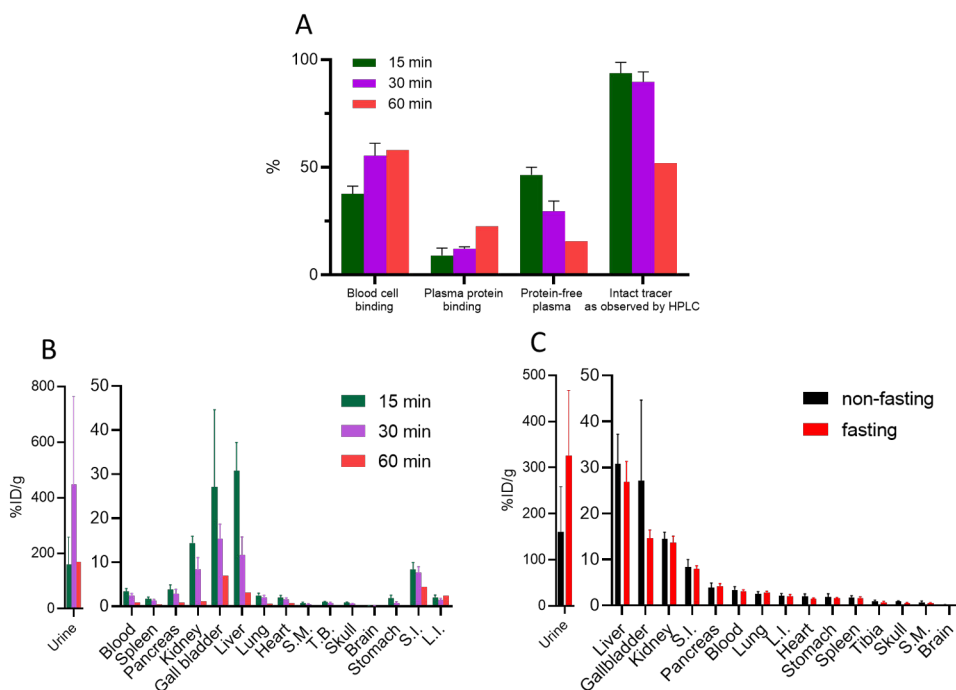
Figure 16. [^{18}F]FDG-Tz *ex vivo* evaluation: radioactivity concentration in blood components at 15 min (n = 3), 30 min (n = 3), and 60 min (n = 2) post-injection (A); *ex vivo* biodistribution in healthy mice at 15 min (n = 6), 30 min (n = 4), and 60 min (n = 2) post-injection (B); *ex vivo* biodistribution in fasted (n=3, 4 hours prior to injection) and non-fasted (n = 6) healthy mice 15 min post-injection (C). (S.M. – skeletal muscle, S.I. – small intestine, L.I. – large intestine)

4.3 Evaluation of structural effects of MSNA after direct labeling with [^{18}F]FDG-Tz

4.3.1 Effect of the backbone and folate moiety on radiolabeled MSNA

4.3.1.1 *In vivo* PET imaging

In Studies II and III, four different MSNA nanostructures were radiolabeled to study the effect of the structural modifications on the biodistribution and to compare them to single-stranded ON (Figure 17). The most outstanding advantage of all MSNAs over the radiolabeled single-stranded ON is a more than three-fold decrease in kidney uptake. In addition, [^{18}F]ON shows high liver accumulation, which is in the same range but with slightly higher values only for [^{18}F]MSNA-PS and [^{18}F]Fol-MSNA-PS, which can be explained by the PS backbone influence. The backbones, either PO or PS, are clear determiners of the elimination route. PO backbone in [^{18}F]MSNA-PO and [^{18}F]Fol-MSNA-PO leads to urinary excretion, while PS structures accumulate in the liver. Prolonged blood circulation results in higher tumor-to-muscle ratios for [^{18}F]MSNA-PS compared to [^{18}F]MSNA-PO or [^{18}F]ON. The addition of folate moiety also increased the tumor-to-muscle ratio, being the highest for [^{18}F]Fol-MSNA-PS (SUV 2.8 ± 0.9 at 60 minutes post-injection).

Figure 17. *In vivo* biological evaluation of MSNA structural effects in HCC1954 tumor-bearing female mice after [18F]ON, [18F]MSNA-PO, [18F]MSNA-PS, [18F]Fol-MSNA-PO, and [18F]Fol-MSNA-PS administration. Maximum intensity projection PET/CT image; T denotes tumor (A); SUV time-activity curves for blood, tumor-to-muscle ratio, kidney, liver, and urine (B).
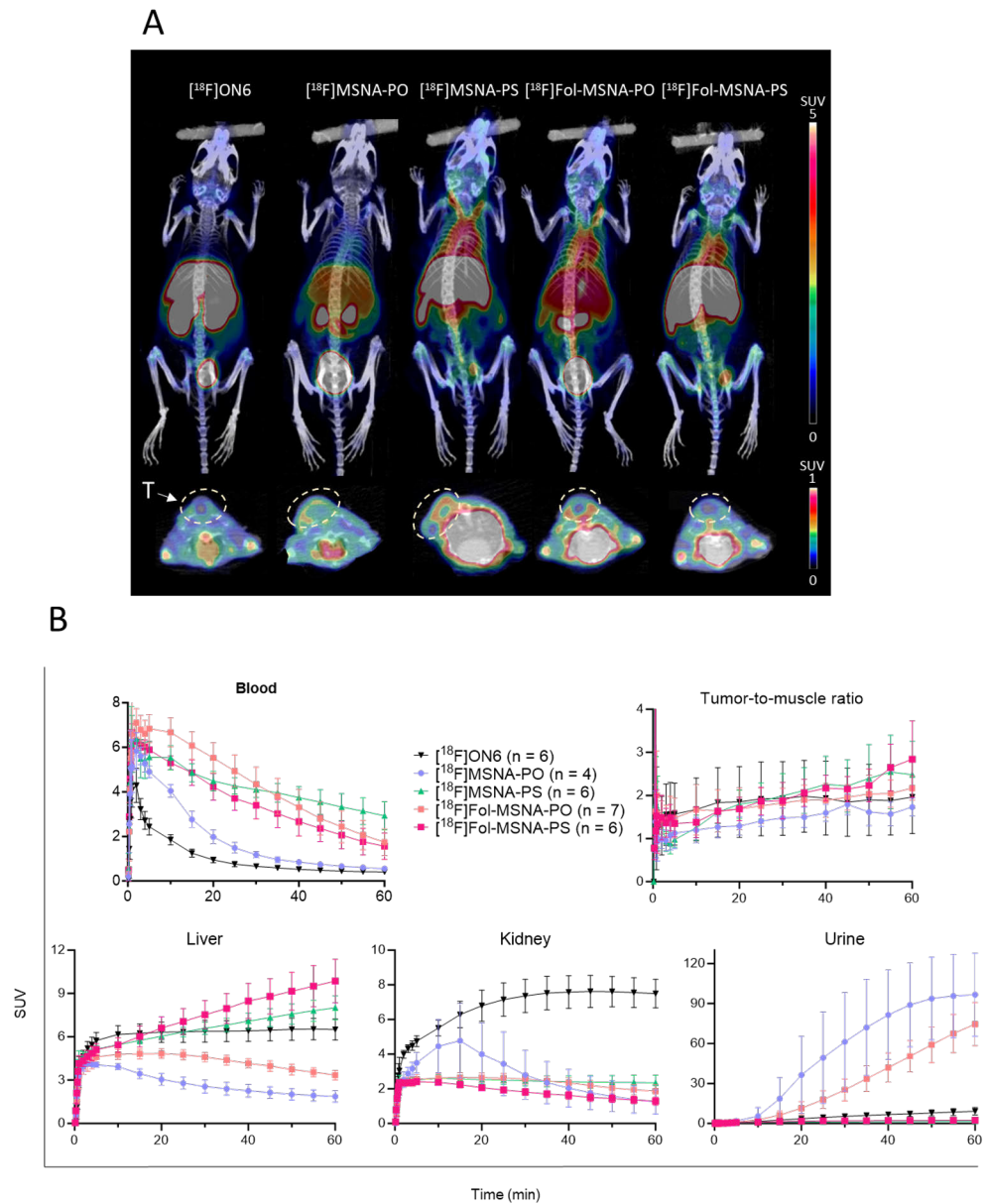
4.3.1.2   *Ex vivo* biodistribution

Ex vivo data shows the same results, highlighting the advantage of MSNAs with lower kidney uptake over linear ON. The %ID/g for [^{18}F]ON at 60 minutes post-injection is 91.0 ± 25.2, while for all radiolabeled MSNAs it stays within the range from 3.6 to 7.1. Additionally, [^{18}F]ON also exhibits the highest undesirable uptake in the abdominal region, such as in the small and large intestines, and the cecum, making it more challenging to analyze PET data.

The FR targeting nature of [^{18}F]Fol-MSNA-PO and [^{18}F]Fol-MSNA-PS could be anticipated from increased liver, kidney, and spleen uptakes compared to non-folate [^{18}F]MSNA-PO and [^{18}F]MSNA-PS structures (Figure 18).
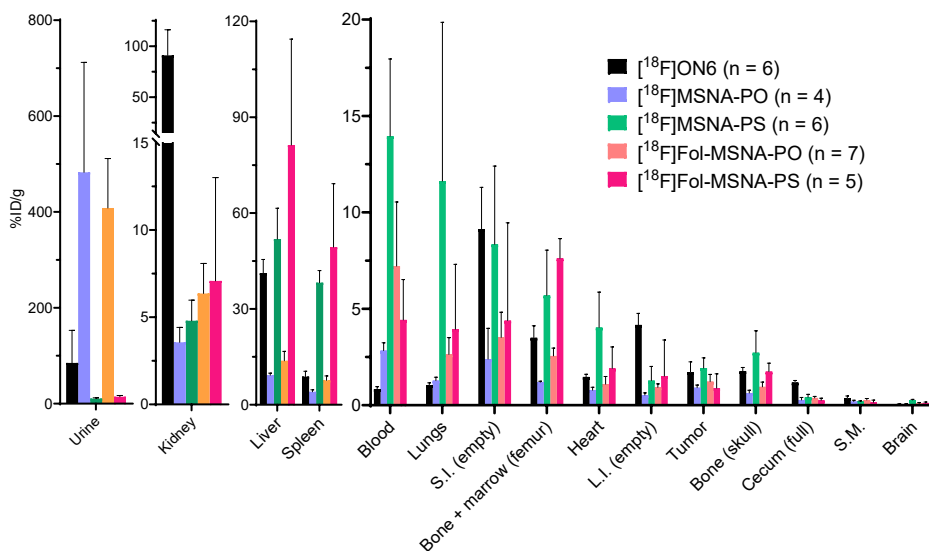
Figure 18. *Ex vivo* biodistribution in HCC1954 tumor-bearing female mice at 60 min post-injection after administrating [^{18}F]ON, [^{18}F]MSNA-PO, [^{18}F]MSNA-PS, [^{18}F]Fol-MSNA-PO, and [^{18}F]Fol-MSNA-PS (S.M. – skeletal muscle, S.I. – small intestine, L.I. – large intestine).

4.3.1.3   *In vitro* folate receptors binding and blocking

The *in vitro* FR binding studies with [^{18}F]FOL, a known tracer for binding FRs, have demonstrated the presence of FRs in HCC1954 tumors. Blocking studies by pre-incubation with Fol-MSNA-PO indicated the specific binding of folate-decorated structures to FRs, resulting in a $96.5\% \pm 0.8$ reduction of [^{18}F]FOL binding (Figure 19).
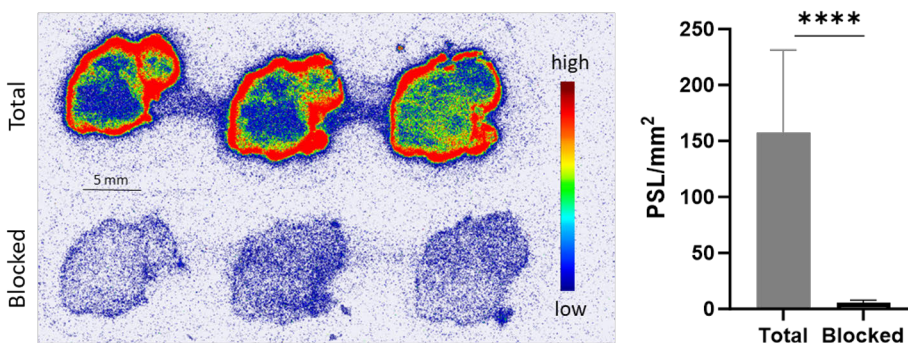
Figure 19. *In vitro* folate receptor binding in HCC1954 tumor cryosections after administrating [^{18}F]FOL. A molar excess of Fol-MSNA-PO was used as a blocking agent. ****$p < 0.0001$.

4.3.2 TCO-load effect on radiolabeled MSNA

4.3.2.1 *In vivo* PET imaging

Three radiolabeled structures with a PS backbone but different TCO-load percentages were investigated *in vivo* (Figure 20). The increase in TCO-load accelerated the blood clearance. TACs curves from Figure 20B, clearly show the rapid decrease in blood uptake of [^{18}F]TCO(400%)-MSNA, already reaching a plateau at 5 minutes, while it takes almost 40 minutes for [^{18}F]TCO(140%)-MSNA to reach a plateau, and [^{18}F]MSNA-PS has a slow blood clearance profile. However, at 60 minutes post- injection, an interesting tendency is observed among the tracers. While generally an increase of TCO-load considerably decreases the blood uptake, further increases of TCO-load slightly increase the radiotracer concentration in the blood at 60 minutes post-injection (blood SUV in increased TCO-load order is 2.9 ± 0.6, 0.3 ± 0.04, and $0.4 \pm + 0.1$). This suggests that the increased number of [^{18}F]FDG-Tz on the surface of the MSNA starts to effect the biodistribution.

The tumor uptake pattern correlates with the blood TACs and connects with the speed of blood clearance of the tracer, being the highest for [^{18}F]MSNA-PS (SUV 0.38 ± 0.17), followed by [^{18}F]TCO(140%)-MSNA (SUV 0.14 ± 0.09), and [^{18}F]TCO(400%)-MSNA (SUV 0.12 ± 0.07). Higher TCO-load increases liver uptake and decreases uptake in the kidney.
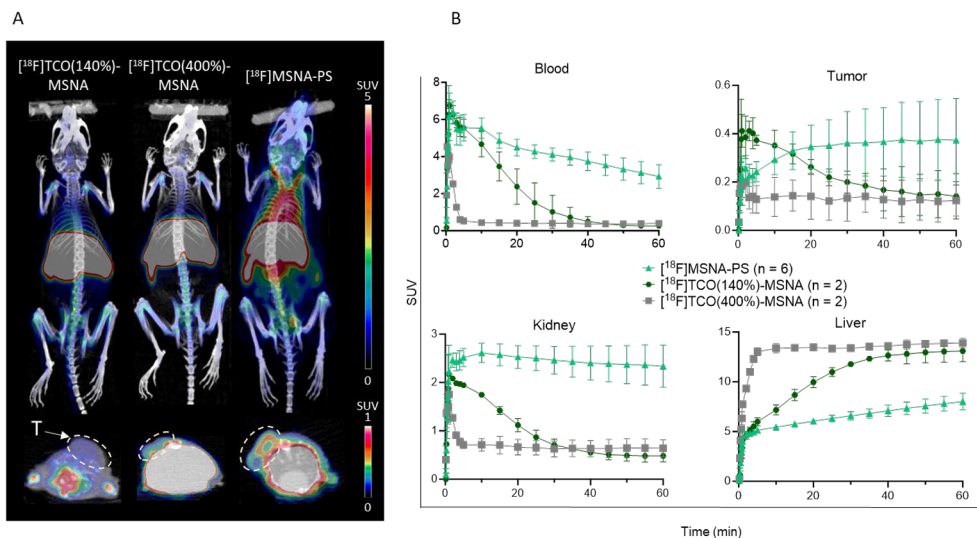
Figure 20. *In vivo* biological evaluation of the TCO-load effect in HCC1954 tumor-bearing female mice after [^{18}F]MSNA-PS, [^{18}F]TCO(140%)-MSNA and [^{18}F]TCO(400%)-MSNA administration. Maximum intensity projection PET/CT images; T denotes tumor (A); SUV time-activity curves for blood, tumor, kidney, and liver (B).

4.3.2.2   *Ex vivo* biodistribution

A higher TCO percentage, resulting in a higher number of [^{18}F]FDG-Tz molecules on the surface, makes the structures more hydrophilic. This results in higher blood, spleen, liver, and lungs uptake between 140% and 400% TCO-load MSNAs, as observed from *ex vivo* results (Figure 21). In the case of monofunctionalized [^{18}F]MSNA-PS, where there is only one [^{18}F]FDG-Tz on the nanostructure surface, it does not affect the biodistribution. Therefore, the biodistribution profiles are primarily determined by the MSNA structure, resulting in high liver and blood uptake, and consequently tumor uptake.
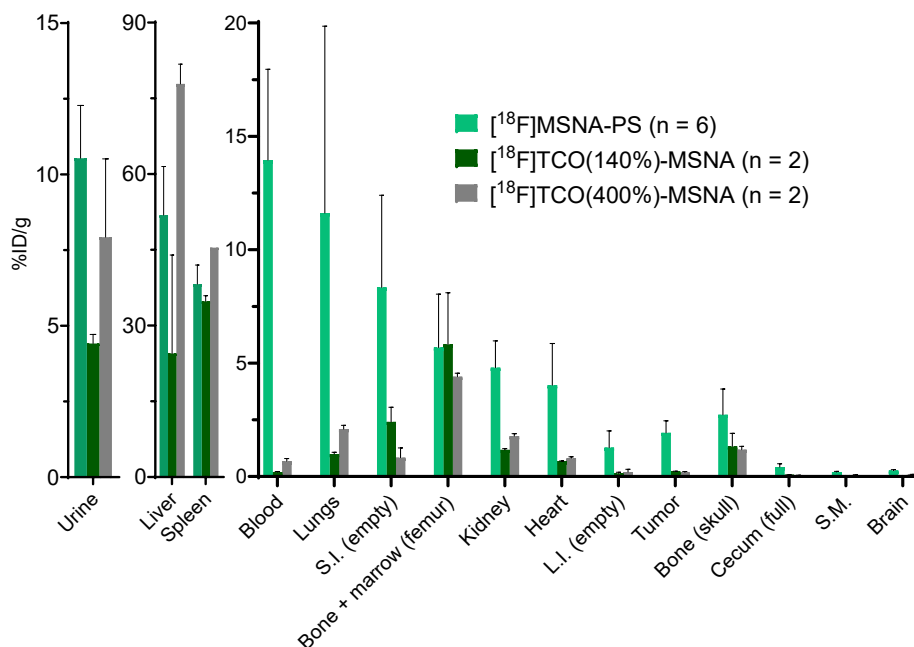
Figure 21. *Ex vivo* biodistribution in HCC1954 tumor-bearing female mice at 60 min post-injection after administrating [^{18}F]MSNA-PS, [^{18}F]TCO(140%)-MSNA, and [^{18}F]TCO(400%)-MSNA (S.M. – skeletal muscle, S.I. – small intestine, L.I. – large intestine).

4.4 Biological evaluation of MSNA by using pretargeted approach

4.4.1 *In vivo* PET imaging

To evaluate the feasibility of [^{18}F]FDG-Tz as a pretargeted agent for biological evaluation of TCO-functionalized MSNA, TCO(140%)-MSNA was injected 20 minutes prior to the tracer administration. Figure 22 represents dynamic PET imaging results for the Study I pretargeted approach in HCC1954 tumor-bearing female mice. The highest tumor accumulation was observed in the pretargeted approach, SUV 0.32 ± 0.14 at 60 minutes post-injection compared to SUV 0.16 ± 0.04 tumor uptake for [^{18}F]FDG-Tz, making it statistically significant with p = 0.04. The higher tumor uptake correlates with the slow blood elimination and shows a five times higher blood uptake at 60 minutes post-injection in the pretargeted experiment. Additionally, the pretargeted approach also highlighted a lower liver accumulation which was almost half less than that found in a comparison to directly labeled MSNA (6.6 ± 0.9 vs. 13.1 ± 1.1).

Figure 22. *In vivo* biological evaluation of pretargeted experiment in HCC1954 tumor-bearing female mice after [18F]FDG-Tz, [18F]TCO(140%)-MSNA, and TCO(140%)-MSNA + [18F]FDG-Tz administration. TCO(140%)-MSNA and [18F]FDG-Tz were injected with a 20-minute lag time. Maximum intensity projection PET/CT images; T denotes tumor (A); SUV time-activity curves for blood, tumor, and liver (B).

4.4.2   *Ex vivo* biodistribution

Figure 23 confirms the favorable results from the pretargeted approach, such as the highest tumor uptake caused by slow blood clearance, which we can also see in the higher heart %ID/g results. The observed elevated uptake in the spleen, liver, and bone + marrow in the pretargeted approach is in good agreement with directly labeled [18F]TCO(140%)-MSNA. However, *ex vivo* results did not provide lower liver accumulation compared to [18F]TCO(140%)-MSNA, which could be explained by the high variation in %ID/g values. Increased uptake in urine for TCO(140%)-MSNA + [18F]FDG-Tz administration compared with [18F]TCO(140%)-MSNA (276.6 ± 163.4 vs 4.4 ± 0.3, respectively), as well as kidney uptake (7.7 ± 4.5 vs 1.2

± 0.1, respectively) could be explained by early time points circulation of some unreacted [18F]FDG-Tz.
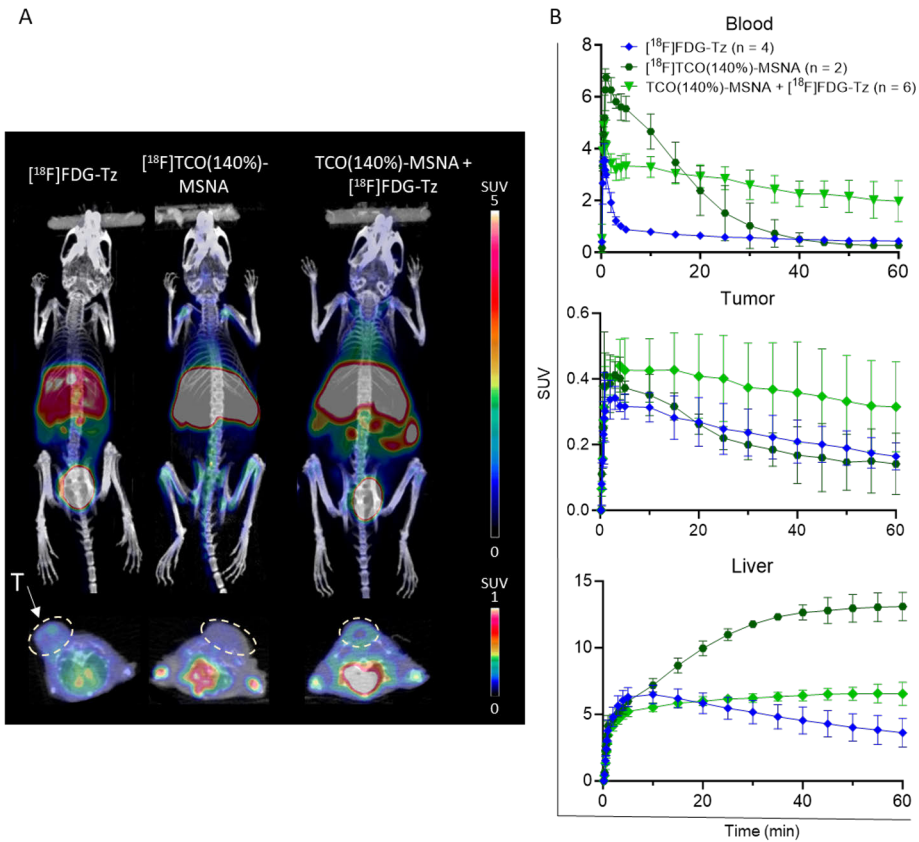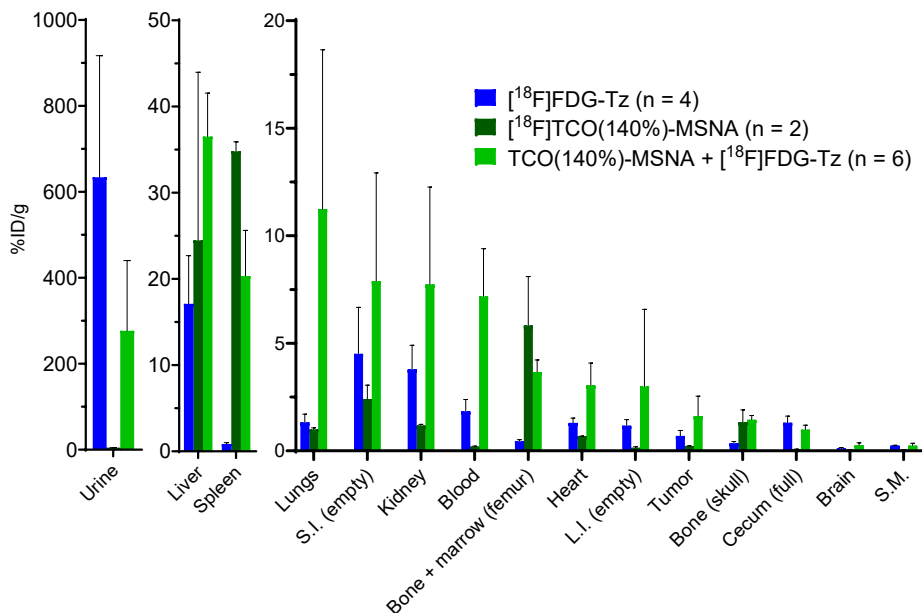

Figure 23. Pretargeted *ex vivo* biodistribution in HCC1954 tumor-bearing female mice at 60 min post-injection after injecting [18F]FDG-Tz, [18F]TCO(140%)-MSNA, and TCO(140%)-MSNA + [18F]FDG-Tz. TCO(140%)-MSNA and [18F]FDG-Tz were injected with a 20-minute lag time (S.M. – skeletal muscle, S.I. – small intestine, L.I. – large intestine).

5   Discussion

5.1   [^{18}F]FDG-Tz as a radiolabeling agent

The utilization of the IEDDA reaction resulted in a great advancement in radiopharmaceutical chemistry both in targeted and pretargeted approaches due to the fast synthesis scheme and use of physiological reaction conditions. However, radiolabeling of tetrazines requires an indirect approach due to its sensitivity to regular fluorination conditions. Nevertheless, this challenge presents an opportunity to modify tetrazine properties favorably during radiolabeling by employing an indirect approach.

Using [^{18}F]FDG as a fluoroglycolization agent is not only necessary from a radiolabeling point of view as an indirect radiolabeling method, but also beneficial from the point of view of production accessibility and property enhancement. However, in this study [^{18}F]FDG-Tz was synthesized starting with mannose triflate as a precursor. Potentially it is possible to use commercially produced [^{18}F]FDG, which is highly available and accessible, after implementing the appropriate purification methods for glucose removal, such as semi-preparative HPLC. This will make [^{18}F]FDG-Tz production faster and easier, which will lead to a potentially better good manufacturing practice (GMP) translation.

Oxime formation between [^{18}F]FDG and tetrazine precursor is generally characterized by good yields. However, it requires acidic conditions and elevated temperatures to promote an acyclic aldehyde form of [^{18}F]FDG. We observed that it is crucial to use freshly prepared anilinium acetate as a buffer to maintain pH. In addition, increasing the temperature from 60°C to 75°C and the addition of methanol during oxime formation improved the reaction yield from 5% to 40%. Methanol or other organic solvent usage in oxime formation is a well-documented approach (X. G. Li et al., 2012); although it is not clear whether the nature of the yield improvement is via increasing solubility or facilitating conjugation.

5.1.1   Pretargeted approach

In Study I, [^{18}F]FDG-Tz was evaluated as a potential agent for pretargeted PET imaging. To validate [^{18}F]FDG as a fluoroglycolization agent, we compared it with

50

[^{18}F]FDR-Tz, which has been previously investigated for pretargeted PET with antibodies (Keinänen, Fung, et al., 2017) and nanoparticles (Keinänen, Mäkilä, et al., 2017). FDG-Tz and FDR-Tz were studied and compared for GLUT1 affinity. The IC$_{50}$ value showed a 15-fold lower affinity to GLUT1 for FDG-Tz compared to FDR-Tz, which is beneficial for a pretargeted agent. A lower affinity indicates reduced binding to GLUT1, as GLUT1 is expressed in erythrocytes, leading to faster blood clearance — an essential criterion for pretargeted experiments, as the prolonged presence of the tracer in the blood lowers the target-to-background contrast for a pretargeted experiment. In addition, a lower GLUT1 affinity leads to lower uptake in GLUT1 rich organs, lowering the background signal as well as the healthy tissue radiation burden. However, *in vitro* cell uptake studies showed concerning results regarding the potential cell uptake of FDG-Tz compared to FDR-Tz, which would be undesirable for extracellular targets.

To confirm or refute [^{18}F]FDG-Tz cell uptake, *in vivo* fasting studies were conducted, revealing no difference in uptake between fasted and non-fasted animals. This suggests that no GLUT1 transportation is occurring *in vivo*. Additionally, this finding is advantageous in terms of animal handling before imaging, as [^{18}F]FDG uptake is known to be influenced by dietary conditions and animal handling (Fueger et al., 2006; Wong et al., 2011).

Furthermore, evaluation in healthy mice showed the absence of GLUT1 transportation with the lack of uptake in GLUT1-rich organs (Elsas & Longo, 1992; Gould & Holman, 1993). As a potential pretargeted agent, [^{18}F]FDG-Tz showed favorable biodistribution in healthy mice, characterized by favorable urinary excretion, fast clearance, and reduced uptake in abdominal region and liver uptake. Compared with previously studied [^{18}F]FDR-Tz (Keinänen et al., 2016), we see the faster blood clearance and notably lower radioactivity in the small and large intestines as advantages of [^{18}F]FDG-Tz. The faster clearance could be explained by the higher number of hydroxyl groups present in the glucose analog compared to the ribose analog, which decreases lipophilicity and facilitates fast clearance and lower accumulation in the abdominal region (Shinde et al., 2021).

5.1.2   Targeted approach

Studies II and III demonstrated that [^{18}F]FDG-Tz is a reliable radiolabeling agent for a variety of TCO-functionalized nanomaterials via an IEDDA reaction under mild conditions. The developed method has proven to be straightforward and reproducible. The structure of MSNAs did not impact the reaction outcome, emphasizing the versatility of this approach. Optimal conditions for the radiolabeling of the IEDDA reaction were determined to be at r.t. with just a 5-minute reaction time. Such short reaction time is a critical benefit in radiosynthesis, where time is of

the essence due to constant decay. Interestingly, increasing the reaction time during the method development did not result in a higher IEDDA yield. Carrying out the reaction under r.t. is also highly beneficial and allows the radiolabeling of sensitive molecules without the need for solvents or catalysts, and without producing any side-products.

The key factor influencing the conversion was found to be the ratio between tetrazine and TCO, with a minimum requirement of a 1:1 ratio and preferably an excess of TCO for complete reaction conversion. However, an excess of TCO-functionalized MSNA is likely to leave some unreacted TCO groups. In the case of monofunctionalized MSNAs, the presence of unreacted TCO-MSNAs in the final solution means lowering molar activity with no or minimum interfering biological behavior of radiolabeled MSNA. However, in the case of MSNAs with a high TCO-load, all the MSNAs would most likely be radiolabeled, and some TCO groups will remain unreacted.

5.2 Structural effects of MSNA after direct labeling with [^{18}F]FDG-Tz

Radiolabeling with [^{18}F]FDG-Tz via the IEDDA reaction enabled the investigation of six MSNA structures *in vivo* and *ex vivo*, facilitating comparison with a radiolabeled single-stranded ON, and enabling the study of the impact of structural modification on their biodistribution. The discussion regarding the influence of structural modifications can be divided into the superiority of MSNA over linear ON, the backbone influence, the folate moiety effect, and the TCO-load influence. Therefore, the following were investigated: two monofunctionalized MSNA structures with PO and PS backbones, two monofunctionalized folate-decorated structures, one with a PO backbone and one with a PS backbone, as well as two MSNA structures with a higher TCO-load.

The selected antisense ON sequence against HER2 mRNA transcript is a model sequence with demonstrated HER2 downregulation (H. Li et al., 2018). In Study II, we confirmed the antisense activity of MSNA-PO and MSNA-PS *in vitro* through a Western blot analysis. However, the *in vivo* internalization of MSNAs is likely to be low. Therefore, for non-folate structures the tumor accumulation is most likely due to the enhanced permeability and retention (EPR) effect, which is common for nanomaterials due to tumor vasculature permeability and lymphatic drainage (Maeda, 2001; Sita et al., 2017; Torchilin, 2011).

As a common trend, we observed the coincidence in all structures of a relatively high uptake in the liver, spleen, and bone + marrow. These are common characteristics of intravenously administered nanomaterials, which are guided into

the mononuclear phagocyte system (MPS), previously known as reticuloendothelial system (RES) (Blanco et al., 2015; Tsoi et al., 2016).

Overall, radiolabeled MSNAs demonstrated favorable biodistribution over single-stranded ON. [^{18}F]ON displayed a notable increase in kidney uptake, along with liver uptake comparable to MSNA structures with a PS backbone. Additionally, it showed the highest radiation concentration in the abdominal region, namely the small and large intestines, and the cecum. As it did not achieve an outstanding tumor or tumor-to-muscle ratio, [^{18}F]ON fell short in comparison to MSNAs due to its high accumulation in non-targeted tissues, which increases the background signal and healthy organ burden.

The quick elimination of [^{18}F]MSNA-PO from the blood is likely attributed to PO backbone degradation *in vivo*. The known method to improve enzymatic stability is to introduce a PS backbone to the structure (Geary et al., 2015; Kyriazi et al., 2022). This modification indeed slowed down blood clearance and consequently slightly increased tumor-to-muscle ratio. However, it also increased liver uptake, a common occurrence with the PS backbone (Crooke et al., 2000; Geary et al., 2015; Miller et al., 2016). Higher radiation concentrations in the lungs, spleen, liver, bone marrow, and ovaries were also previously reported for PS structures (Braasch et al., 2004; Geary et al., 2015), which is in good agreement with our findings. By comparing PO and PS regular and folate-decorated structures, we observed that the elimination route was determined by the backbone.

The attempt to introduce a targeting moiety resulted in folate-decorated MSNA structures with natural PO and PS backbones. Both structures resulted in an increased uptake observed in the liver, kidneys, spleen, and tumor-to-muscle ratios. These changes in biodistribution are in line with general tendencies dedicated to FR binding, particularly given the elevated expression of FRs in the kidneys (Parker et al., 2005). FR binding was confirmed with *in vitro* blocking studies in tumor cryosections. A known tracer to bind FRs, [^{18}F]FOL, confirmed the presence of FR-positive cells in HCC1954 tumors, and was suitably blocked by Fol-MSNA-PO, signaling the FR binding nature of the biodistribution of this MSNA.

Not only will modifications made by changing the backbone or adding targeting moiety affect the MSNA, but the surface chemistry will also influence the fate of the particles *in vivo*. Therefore, we further investigated the effect of an increased amount of TCO on the *in vivo* biodistribution by radiolabeling MSNAs with a 25%, 140%, and 400% TCO-load, where the 25% TCO-load represents monofunctionalized MSNA with TCO attached only to one arm out of twelve for every fourth MSNA molecule. All structures had a PS backbone for proper comparison.

An increased amount of TCO led to an increased number of [^{18}F]FDG-Tz and unreacted TCO groups on the MSNA surface. This differs from monofunctionalized MSNAs, where structures either have one arm radiolabeled with [^{18}F]FDG-Tz or one

arm with an unreacted TCO group, with the last one being invisible in PET imaging. We hypothesized that monofunctionalization of MSNA with [18F]FDG-Tz would not interfere with its biological behavior. Thus, we should look at the biodistribution from the perspective that as soon as we increase the TCO-load to 140%, the biodistribution starts to be affected by surface functionalization, including both excess of unreacted TCO groups and [18F]FDG-Tz. This resulted in a notable difference in organ accumulation, namely blood, plasma, lungs, and tumor between [18F]MSNA-PS and MSNAs with a high TCO-load. With a further increase in the TCO-load from 140% to 400% we observe a tendency towards an increased uptake in the blood, lungs, and kidneys due to the altered hydrophilicity of the surface. For MSNAs with 140% and 400% TCO-load, the TACs indicated a more dominant liver uptake starting from early time points, with tracers being harvested by the liver and demonstrating a mirror pattern of the blood uptake. In addition, *ex vivo* data for bone + marrow and spleen were not notably affected by the TCO-load; possibly explained by the recognition of MSNAs by the MPS regardless of the TCO percentage load.

The results discussed above emphasize the importance and possibility of affecting *in vivo* behavior by adjusting the surface of MSNAs. However, the limitations of the presented results include a low number of animals per studied tracer.

5.3   Pretargeted PET of MSNA

[18F]FDG-Tz successfully tracked TCO-functionalized MSNA *in vivo* in tumor-bearing mice with a pretargeted approach with a 20-minute lag time between injections. The pretargeted approach exhibited the highest tumor uptake which correlates with the slowest blood clearance. Similar to directly labeled non-folate MSNAs, discussed in the previous chapter, tumor accumulation for both the targeted and pretargeted approaches is likely caused by the EPR effect, along with increased uptake in the liver, spleen, and bone + marrow caused by MPS compared to [18F]FDG-Tz.

However, evaluation of the structures using targeted and pretargeted approaches does not show exactly the same biodistribution profiles. For example, the pretargeted approach stands out as having considerably higher radiation concentrations in blood, plasma, tumor, and lungs. Our results suggest a notably lower concentration of directly labeled [18F]TCO(140%)-MSNAs in both blood and plasma compared to pretargeted radiolabeled TCO(140%)-MSNA, which cannot be attributed to [18F]FDG-Tz, as it quickly eliminates from the bloodstream. This difference in biodistribution can be attributed to variations in the surface chemistry of MSNAs. In the case of [18F]TCO(140%)-MSNA, the surface of the structure contains both TCO groups, which are radiolabeled with [18F]FDG-Tz, and unreacted TCO groups. On

the other hand, in the pretargeted approach TCO(140%)-MSNA with free TCO groups on the surface is administrated and distributed *in vivo*. This difference in surface chemistry may influence the protein corona around the MSNA, consequently affecting their *in vivo* behavior. This observation also aligns with earlier discussion regarding the influence of the different TCO-load on the biodistribution due to altered hydrophilicity of the surface.

The limitation of this study is the short lag time of 20 minutes between injections. While it was sufficient to demonstrate the feasibility of the bioorthogonal reaction and pretargeted approach as a concept, the relatively high radioactivity in the blood 60 minutes post-injection suggests the need for a longer gap between the MSNA and the radiotracer injection. This adjustment may likely lead to an increase in tumor uptake.

6   Conclusions

In Study I, [^{18}F]FDG-Tz was biologically evaluated in healthy mice and identified as a promising candidate for pretargeted PET imaging with favorable pharmacokinetics characterized by fast blood clearance and urinary excretion, thus demonstrating its advantages over [^{18}F]FDR-Tz.

In Studies I, II, and III, [^{18}F]FDG-Tz was applied as a radiolabeling agent for targeted PET imaging of a variety of MSNA structures via the IEDDA reaction. The methods proved to be straightforward and reproducible, achieving conversion yields of up to 100%. This enabled to study the influence of the structural effect on the biological behaviour of MSNA. TCO-functionalized MSNA structures with either PO or PS backbones were successfully radiolabeled with [^{18}F]FDG-Tz and compared with single-stranded radiolabeled ON. The evaluation in tumor-bearing mice demonstrated the advantageous biodistribution of the MSNAs over linear ON. Additionally, MSNA with PS backbone showed prolonged blood circulation and the highest tumor uptake. The backbone was also shown to influence the elimination route. Folate-decorated MSNAs with either PO or PS backbones were radiolabeled and compared with non-folate structures. The addition of the folate moiety demonstrated to be a feasible step for targeting purposes by showing an increased uptake in FR-related organs. In addition, Fol-MSNA-PO blocked a known tracer to bind FRs, [^{18}F]FOL, *in vitro*. [^{18}F]Fol-MSNA-PS showed the highest tumor-to-muscle ratio among the radiolabeled compounds. The effect of the MSNA surface was evaluated using radiolabeled structures with different TCO-load.

Finally, [^{18}F]FDG-Tz successfully tracked *in vivo* TCO-functionalized MSNA in a pretargeted approach with a 20-minute lag time, showing the highest tumor uptake compared to [^{18}F]FDG-Tz and directly labeled MSNA.

Acknowledgements

I wish to express my gratitude to Professor Tapani Viitala from Åbo Akademi/University of Helsinki and Assistant Professor Umberto Battisti from the University of Copenhagen, who were pre-examiners of this thesis. Your expertise, valuable feedback, and critical comments improved my thesis. I am honored by the acceptance of Assistant Professor Verena Pichler from the University of Vienna to be my esteemed opponent. Thank you for finding the time to challenge this work.

I owe my deepest gratitude to my supervisors, Professor Anu J. Airaksinen and Assistant Professor Xiang-Guo Li. Your continuous support, encouragement, and guidance throughout my PhD journey made it easier and more enjoyable. Thank you for instilling great radiation safety habits in me with your examples. Anu, thank you for helping me develop a big-picture vision and a positive learning attitude towards criticism. Xiang, thank you for taking the time to share your practical skills with great kindness, patience, and understanding.

I want to thank my follow-up committee members, Associate Professor Filip Ekholm and Adjunct Professor Sarita Forsback, for their support, honesty, and encouraging words. Sarita, I also owe you my deepest gratitude for including me in the RK2 family and giving me the opportunity to learn GMP production.

Collaborations in PET studies are extensive and require a team of professionals. My thanks to Professor Anne Roivainen and Professor Pasi Virta for their collaboration and expertise. Your incredibly fast responses and thorough explanations were invaluable. I want to thank Heidi Liljenbäck, for always being there for animal-related processes and special appreciation for enjoyable lunches and all work events moments. Aake Honkaniemi, thank you for your help and patience in organizing and supporting preclinical studies. The contribution of all co-authors, collaborators, and colleagues is thoroughly appreciated, including Juulia Järvinen, Professor Jarkko Rautio, Johan Rajander, Imran Igbal, Jyrki Lehtimäki, Harri Salo,

Erica Nyman, Marja-Riitta Kajaala. Luciana Kovacs, thank you for your company and conversations. Special thanks to Antti Äärelä for the smooth collaboration and Olli Moisio for sharing the struggle. I sincerely thank Risto Savela, your help is deeply appreciated, and backup career farming plan conversations were enjoyable. Aurum people, PET-pals, and PETknits fellows, including but not limited to Pyry Dillemuth, Jesse Ponkamo, Jonne Kunnas, Marjo Nylund, Putri Andriana, Negar Akbari Samani, Sami Paunonen, Petteri Lövdahl, and Xiaoqing Zhuang, thank you for the shared moments and lovely company. A special thanks to Erika Atencio Herre for all the therapeutic lunches, events, memories, and the amazing prize-winning unforgettable elevator video shooting.

I want to thank the RK2 team for your friendliness and readiness to help. Some, who were not mentioned yet, but not all, are Noora Rajala, Simo Salo, Edla Kerminen, Thomas Keller, Saga Grönfors, Olli Eskola, Margit Åhman-Kantola, Esa Kokkomäki, Aleksi Vianto, Nina Lauren, Professor Olof Solin, and Semi Helin. Adjunct Professor Anna Kirjavainen, your email was a light at the end of the tunnel. I also want to thank my Helsinki colleagues, Anisa Biti, Alessia Centanni, and Surachet Imlimthan for sharing professional and personal memories. I wish to thank everyone I met on my journey for their kindness and time.

I am grateful for my family and friends. I want to thank my parents, Sviatlana and Mikalai, for their unconditional love and support. The biggest thanks go to my sister, Alena, for listening to all my complaints, and exciting, sad, and happy news. Vita, you cannot be understated for your time, company, and help with Viiru. My friends in Belarus, Vika and Maksim, thank you for being supportive even from afar. I want to thank Viiru, who always ensured I finished work on time for our evening walks. My warmest thanks go to Artsiom for caring, "jackpot", "a big catch", and for some very important words in my life.

Finally, I want to thank myself.

Turku, June 2024

Tatsiana Auchynnikava

List of References

Agard, N. J., Prescher, J. A., & Bertozzi, C. R. (2004). A strain-promoted [3 + 2] azide-alkyne cycloaddition for covalent modification of biomolecules in living systems. *Journal of the American Chemical Society*, *126*(46), 15046–15047.

Al Jammaz, I., Al-Otaibi, B., Amer, S., Al-Hokbany, N., & Okarvi, S. (2012). Novel synthesis and preclinical evaluation of folic acid derivatives labeled with [18]F-[FDG] for PET imaging of folate receptor-positive tumors. *Nuclear Medicine and Biology*, *39*(6), 864–870.

Altai, M., Membreno, R., Cook, B., Tolmachev, V., & Zeglis, B. M. (2017). Pretargeted imaging and therapy. *Journal of Nuclear Medicine*, *58*(10), 1553–1559.

Amantana, A., & Iversen, P. L. (2005). Pharmacokinetics and biodistribution of phosphorodiamidate morpholino antisense oligomers. *Current Opinion in Pharmacology*, *5*(5), 550–555.

Ametamey, S. M., Honer, M., & Schubiger, P. A. (2008). Molecular imaging with PET. *Chemical Reviews*, *108*(5), 1501–1516.

Arja, K., Elgland, M., Appelqvist, H., Konradsson, P., Lindgren, M., & Nilsson, K. P. R. (2018). Synthesis and Characterization of Novel Fluoro-glycosylated Porphyrins that can be Utilized as Theranostic Agents. *ChemistryOpen*, *7*(7), 495–503.

Au, K. M., Tripathy, A., Lin, C. P. I., Wagner, K., Hong, S., Wang, A. Z., & Park, S. I. (2018). Bespoke Pretargeted Nanoradioimmunotherapy for the Treatment of Non-Hodgkin Lymphoma. *ACS Nano*, *12*(2), 1544–1563.

Auchynnikava, T., Äärelä, A., Liljenbäck, H., Järvinen, J., Andriana, P., Kovacs, L., Rautio, J., Rajander, J., Virta, P., Roivainen, A., Li, X. G., & Airaksinen, A. J. (2023). Tetrazine Glycoconjugate for Pretargeted Positron Emission Tomography Imaging of trans-Cyclooctene-Functionalized Molecular Spherical Nucleic Acids. *ACS Omega*, *8*(48), 45326–45336.

Azad, B. B., Chirakal, R., & Schrobilgen, G. J. (2007). Trifluoromethanesulfonic acid, an alternative solvent medium for the direct electrophilic fluorination of DOPA: new syntheses of 6-[18F]fluoro-L-DOPA and 6-[18F]fluoro-D-DOPA. *Journal of Labelled Compounds and Radiopharmaceuticals*, *50*(14), 1236–1242.

Banerjee, A., Maschauer, S., Hübner, H., Gmeiner, P., & Prante, O. (2013). Click chemistry based synthesis of dopamine D4 selective receptor ligands for the selection of potential PET tracers. *Bioorganic & Medicinal Chemistry Letters*, *23*(22), 6079–6082.

Bergman, J., & Solin, O. (1997). Fluorine-18-labeled fluorine gas for synthesis of tracer molecules. *Nuclear Medicine and Biology*, *24*(7), 677–683.

Beyerlein, F., Piel, M., Höhnemann, S., & Rösch, F. (2013). Automated synthesis and purification of [18F]fluoro-[di-deutero]methyl tosylate. *Journal of Labelled Compounds and Radiopharmaceuticals*, *56*(7), 360–363.

Blackman, M. L., Royzen, M., & Fox, J. M. (2008). Tetrazine ligation: Fast bioconjugation based on inverse-electron-demand Diels-Alder reactivity. *Journal of the American Chemical Society*, *130*(41), 13518–13519.

Blanco, E., Shen, H., & Ferrari, M. (2015). Principles of nanoparticle design for overcoming biological barriers to drug delivery. *Nature Biotechnology 2015 33:9*, *33*(9), 941–951.

Bousmail, D., Amrein, L., Fakhoury, J. J., Fakih, H. H., Hsu, J. C. C., Panasci, L., & Sleiman, H. F. (2017). Precision spherical nucleic acids for delivery of anticancer drugs. *Chemical Science*, *8*(9), 6218–6229.

Braasch, D. A., Paroo, Z., Constantinescu, A., Ren, G., Öz, O. K., Mason, R. P., & Corey, D. R. (2004). Biodistribution of phosphodiester and phosphorothioate siRNA. *Bioorganic & Medicinal Chemistry Letters*, *14*(5), 1139–1143.

Chausse, G., Benard, F., Harsini, S., Pan, J., Saprunoff, H., Uribe, C., Allan, H., Perrin, D., Lin, K.-S., & Wilson, D. (2022). First-in-Human Clinical trial of [^{18}F]AMBF$_3$-TATE for PET imaging of neuroendocrine tumors. *Journal of Nuclear Medicine*, *63*(2), 2270.

Cherry, S. R., & Dahlbom, M. (2006). *PET : physics, instrumentation, and scanners*. Springer.

Coenen, H. H. (2007). Fluorine-18 labeling methods: Features and possibilities of basic reactions. In *PET Chemistry: The driving force in molecular imaging* (pp. 15–50). Springer.

Conti, M., & Eriksson, L. (2016). Physics of pure and non-pure positron emitters for PET: A review and a discussion. *EJNMMI Physics*, *3*(8), 1–17.

Crooke, R. M., Graham, M. J., Martin, M. J., Lemonidis, K. M., Wyrzykiewiecz, T., & Cummins, L. L. (2000). Metabolism of antisense oligonucleotides in rat liver homogenates. *Journal of Pharmacology and Experimental Therapeutics*, *292*(1), 140–149.

Debets, M. F., Prins, J. S., Merkx, D., Van Berkel, S. S., Van Delft, F. L., Van Hest, J. C. M., & Rutjes, F. P. J. T. (2014). Synthesis of DIBAC analogues with excellent SPAAC rate constants. *Organic & Biomolecular Chemistry*, *12*(27), 5031–5037.

Deng, X., Rong, J., Wang, L., Vasdev, N., Zhang, L., Josephson, L., & Liang, S. H. (2019). Chemistry for Positron Emission Tomography: Recent Advances in ^{11}C-, ^{18}F-, ^{13}N-, and ^{15}O-Labeling Reactions. *Angewandte Chemie International Edition*, *58*(9), 2580–2605.

Devaraj, N. K., Weissleder, R., & Hilderbrand, S. A. (2008). Tetrazine-based cycloadditions: Application to pretargeted live cell imaging. *Bioconjugate Chemistry*, *19*(12), 2297–2299.

Elsas, L. J., & Longo, N. (1992). Glucose transporters. *Annual Review of Medicine*, *43*(1), 377–393.

Fehr, J. M., Myrthil, N., Garrison, A. L., Price, T. W., Lopez, S. A., & Jasti, R. (2023). Experimental and theoretical elucidation of SPAAC kinetics for strained alkyne-containing cycloparaphenylenes. *Chemical Science*, *14*(11), 2839–2848.

Fischer, C. R., Groehn, V., Reber, J., Schibli, R., Ametamey, S. M., & Müller, C. (2013). Improved PET imaging of tumors in mice using a novel ^{18}F-folate conjugate with an albumin-binding entity. *Molecular Imaging and Biology*, *15*(6), 649–654.

Fischer, C. R., Müller, C., Reber, J., Müller, A., Krämer, S. D., Ametamey, S. M., & Schibli, R. (2012). [^{18}F]fluoro-deoxy-glucose folate: A novel PET radiotracer with improved in vivo properties for folate receptor targeting. *Bioconjugate Chemistry*, *23*(4), 805–813.

Fueger, B. J., Czernin, J., Hildebrandt, I., Tran, C., Halpern, B. S., Stout, D., Phelps, M. E., & Weber, W. A. (2006). Impact of Animal Handling on the Results of ^{18}F-FDG PET Studies in Mice. *Journal of Nuclear Medicine*, *47*(6), 999–1007.

García-Vázquez, R., Battisti, U. M., & Herth, M. M. (2022). Recent Advances in the Development of Tetrazine Ligation Tools for Pretargeted Nuclear Imaging. *Pharmaceuticals*, *15*(6), 685.

García-Vázquez, R., Jørgensen, J. T., Bratteby, K. E., Shalgunov, V., Hvass, L., Herth, M. M., Kjær, A., & Battisti, U. M. (2022). Development of ^{18}F-Labeled Bispyridyl Tetrazines for In Vivo Pretargeted PET Imaging. *Pharmaceuticals*, *15*(2), 245.

Geary, R. S., Norris, D., Yu, R., & Bennett, C. F. (2015). Pharmacokinetics, biodistribution and cell uptake of antisense oligonucleotides. *Advanced Drug Delivery Reviews*, *87*, 46–51.

Goodwin, D., Meares, C., McCall, M., McTigue, M., & Chaovapong, W. (1988). Pre-targeted immunoscintigraphy of murine tumors with indium-111-labeled bifunctional haptens. *Journal of Nuclear Medicine*, *29*(2), 226–234.

Gould, G. W., & Holman, G. D. (1993). The glucose transporter family: Structure, function and tissue-specific expression. *Biochemical Journal*, *295*(2), 329–341.

Gulumkar, V., Äärelä, A., Moisio, O., Rahkila, J., Tähtinen, V., Leimu, L., Korsoff, N., Korhonen, H., Poijärvi-Virta, P., Mikkola, S., Nesati, V., Vuorimaa-Laukkanen, E., Viitala, T., Yliperttula, M., Roivainen, A., & Virta, P. (2021). Controlled Monofunctionalization of Molecular Spherical Nucleic Acids on a Buckminster Fullerene Core. *Bioconjugate Chemistry*, *32*(6), 1130–1138.

Hamacher, K., Coenen, H. H., & Stocklin, G. (1986). Efficient stereospecific synthesis of no-carrier-added 2-[18F]-fluoro-2-deoxy-D-glucose using aminopolyether supported nucleophilic substitution. *Journal of Nuclear Medicine*, *27*(2), 235–239.

Handula, M., Chen, K.-T., Seimbille, Y., Thomas, J., Joseph, N., & Eremin, D. (2021). IEDDA: An Attractive Bioorthogonal Reaction for Biomedical Applications. *Molecules*, *26*(15), 4640.

Hou, S., Choi, J. S., Garcia, M. A., Xing, Y., Chen, K. J., Chen, Y. M., Jiang, Z. K., Ro, T., Wu, L., Stout, D. B., Tomlinson, J. S., Wang, H., Chen, K., Tseng, H. R., & Lin, W. Y. (2016). Pretargeted positron emission tomography imaging that employs supramolecular nanoparticles with in vivo bioorthogonal chemistry. *ACS Nano*, *10*(1), 1417–1424.

Houghton, J. L., Membreno, R., Abdel-Atti, D., Cunanan, K. M., Carlin, S., Scholz, W. W., Zanzonico, P. B., Lewis, J. S., & Zeglis, B. M. (2017). Establishment of the in vivo efficacy of pretargeted radioimmunotherapy utilizing inverse electron demand diels-alder click chemistry. *Molecular Cancer Therapeutics*, *16*(1), 124–133.

Hugenberg, V., Breyholz, H. J., Riemann, B., Hermann, S., Schober, O., Schäfers, M., Gangadharmath, U., Mocharla, V., Kolb, H., Walsh, J., Zhang, W., Kopka, K., & Wagner, S. (2012). A new class of highly potent matrix metalloproteinase inhibitors based on triazole-Substituted hydroxamates: (Radio)synthesis and in vitro and first in vivo evaluation. *Journal of Medicinal Chemistry*, *55*(10), 4714–4727.

Huisgen, R. (1963). 1,3-Dipolar Cycloadditions. Past and Future. *Angewandte Chemie International Edition*, *2*(10), 565–598.

Hultsch, C., Schottelius, M., Auernheimer, J., Alke, A., & Wester, H. J. (2009). 18F-Fluoroglucosylation of peptides, exemplified on cyclo(RGDfK). *European Journal of Nuclear Medicine and Molecular Imaging*, *36*(9), 1469–1474.

Ilhan, H., Todica, A., Lindner, S., Boening, G., Gosewisch, A., Wängler, C., Wängler, B., Schirrmacher, R., & Bartenstein, P. (2019). First-in-human 18F-SiFAlin-TATE PET/CT for NET imaging and theranostics. *European Journal of Nuclear Medicine and Molecular Imaging*, *46*(11), 2400–2401.

Jacobson, O., Kiesewetter, D. O., & Chen, X. (2015). Fluorine-18 radiochemistry, labeling strategies and synthetic routes. *Bioconjugate Chemistry*, *26*(1), 1–18.

Ji, P., Atherton, J. H., & Page, M. I. (2012). Copper catalysed azide– alkyne cycloaddition (CuAAC) in liquid ammonia. *Organic & Biomolecular Chemistry*, *10*(39), 7965–7969.

Kalofonos, H., Rusckowski, M., Siebecker, D., Sivolapenko, G., Snook, D., Lavender, J., Epenetos, A., & Hnatowich, D. (1990). Imaging of tumor in patients with indium-111-labeled biotin and streptavidin-conjugated antibodies: preliminary communication. *Journal of Nuclear Medicine*, *31*, 1791–1796.

Karacay, H., Sharkey, R. M., McBride, W. J., Rossi, E. A., Chang, C. H., & Goldenberg, D. M. (2011). Optimization of Hapten-Peptide Labeling for Pretargeted ImmunoPET of Bispecific Antibody Using Generator-Produced 68Ga. *Journal of Nuclear Medicine*, *52*(4), 555–559.

Keinänen, O., Brennan, J. M., Membreno, R., Fung, K., Gangangari, K., Dayts, E. J., Williams, C. J., & Zeglis, B. M. (2019). Dual Radionuclide Theranostic Pretargeting. *Molecular Pharmaceutics*, *16*(10), 4416–4421.

Keinänen, O., Fung, K., Pourat, J., Jallinoja, V., Vivier, D., Pillarsetty, N. V. K., Airaksinen, A. J., Lewis, J. S., Zeglis, B. M., & Sarparanta, M. (2017). Pretargeting of internalizing trastuzumab and cetuximab with a 18F-tetrazine tracer in xenograft models. *EJNMMI Research*, *7*(95).

Keinänen, O., Li, X. G., Chenna, N. K., Lumen, D., Ott, J., Molthoff, C. F. M., Sarparanta, M., Helariutta, K., Vuorinen, T., Windhorst, A. D., & Airaksinen, A. J. (2016). A New Highly Reactive and Low Lipophilicity Fluorine-18 Labeled Tetrazine Derivative for Pretargeted PET Imaging. *ACS Medicinal Chemistry Letters*, *7*(1), 62–66.

Keinänen, O., Mäkilä, E. M., Lindgren, R., Virtanen, H., Liljenbäck, H., Oikonen, V., Sarparanta, M., Molthoff, C., Windhorst, A. D., Roivainen, A., Salonen, J. J., & Airaksinen, A. J. (2017). Pretargeted PET Imaging of trans-Cyclooctene-Modified Porous Silicon Nanoparticles. *ACS Omega*, *2*(1), 62–69.

Keinänen, O., Partelová, D., Alanen, O., Antopolsky, M., Sarparanta, M., & Airaksinen, A. J. (2018). Efficient cartridge purification for producing high molar activity ^{18}F-glycoconjugates via oxime formation. *Nuclear Medicine and Biology*, *67*, 27–35.

Klein, P. J., Christiaans, J. A. M., Metaxas, A., Schuit, R. C., Lammertsma, A. A., Van Berckel, B. N. M., & Windhorst, A. D. (2015). Synthesis, structure activity relationship, radiolabeling and preclinical evaluation of high affinity ligands for the ion channel of the N-methyl-d-aspartate receptor as potential imaging probes for positron emission tomography. *Bioorganic & Medicinal Chemistry*, *23*(5), 1189–1206.

Knall, A. C., & Slugovc, C. (2013). Inverse electron demand Diels–Alder (iEDDA)-initiated conjugation: a (high) potential click chemistry scheme. *Chemical Society Reviews*, *42*(12), 5131–5142.

Kolb, H. C., Finn, M. G., & Sharpless, K. B. (2001). Click Chemistry: Diverse Chemical Function from a Few Good Reactions. *Angewandte Chemie International Edition*, *40*(11), 2004–2021.

Kontermann, R. E., & Brinkmann, U. (2015). Bispecific antibodies. *Drug Discovery Today*, *20*(7), 838–847.

Krzyczmonik, A., Keller, T., Kirjavainen, A. K., Forsback, S., & Solin, O. (2017). Vacuum ultraviolet photon–mediated production of [^{18}F]F$_2$. *Journal of Labelled Compounds and Radiopharmaceuticals*, *60*(4), 186–193.

Kyriazi, M. E., El-Sagheer, A. H., Medintz, I. L., Brown, T., & Kanaras, A. G. (2022). An Investigation into the Resistance of Spherical Nucleic Acids against DNA Enzymatic Degradation. *Bioconjugate Chemistry*, *33*(1), 219–225.

Laboratoire National Henri Becquerel. (n.d.). Retrieved March 22, 2024, from http://www.lnhb.fr/home/nuclear-data/nuclear-data-table/

Lee, D. E., Na, J. H., Lee, S., Kang, C. M., Kim, H. N., Han, S. J., Kim, H., Choe, Y. S., Jung, K. H., Lee, K. C., Choi, K., Kwon, I. C., Jeong, S. Y., Lee, K. H., & Kim, K. (2013). Facile method to radiolabel glycol chitosan nanoparticles with ^{64}Cu via copper-free click chemistry for MicroPET imaging. *Molecular Pharmaceutics*, *10*(6), 2190–2198.

Lee, S. B., Kim, H. L., Jeong, H.-J., Lim, S. T., Sohn, M.-H., & Kim, D. W. (2013). Mesoporous Silica Nanoparticle Pretargeting for PET Imaging Based on a Rapid Bioorthogonal Reaction in a Living Body. *Angewandte Chemie*, *125*(40), 10743–10746.

Lee, W., Sarkar, S., Pal, R., Kim, J. Y., Park, H., Huynh, P. T., Bhise, A., Bobba, K. N., Kim, K. Il, Ha, Y. S., Soni, N., Kim, W., Lee, K., Jung, J. M., Rajkumar, S., Lee, K. C., & Yoo, J. (2021). Successful Application of CuAAC Click Reaction in Constructing ^{64}Cu-Labeled Antibody Conjugates for Immuno-PET Imaging. *ACS Applied Bio Materials*, *4*(3), 2544–2557.

Li, H., Zhang, B., Lu, X., Tan, X., Jia, F., Xiao, Y., Cheng, Z., Li, Y., Silva, D. O., Schrekker, H. S., Zhang, K., & Mirkin, C. A. (2018). Molecular spherical nucleic acids. *Proceedings of the National Academy of Sciences*, *115*(17), 4340–4344.

Li, X. G., Haaparanta, M., & Solin, O. (2012). Oxime formation for fluorine-18 labeling of peptides and proteins for positron emission tomography (PET) imaging: A review. *Journal of Fluorine Chemistry*, *143*, 49–56.

Li, X. G., Helariutta, K., Roivainen, A., Jalkanen, S., Knuuti, J., & Airaksinen, A. J. (2014). Using 5-deoxy-5-[^{18}F]fluororibose to glycosylate peptides for positron emission tomography. *Nature Protocols*, *9*(1), 138–145.

Li, X., Huang, Q., Xiao, J., Liu, G., Dou, S., Rusckowski, M., Shi, H., Liu, Y., & Cheng, D. (2015). Novel DNA polymer for amplification pretargeting. *ACS Medicinal Chemistry Letters*, *6*(9), 972–976.

Lin, F. L., Hoyt, H. M., Van Halbeek, H., Bergman, R. G., & Bertozzi, C. R. (2005). Mechanistic investigation of the Staudinger ligation. *Journal of the American Chemical Society*, *127*(8), 2686–2695.

Liu, M., Wang, F., Zhang, X., Mao, X., Wang, L., Tian, Y., Fan, C., & Li, Q. (2021). Tracking endocytosis and intracellular distribution of spherical nucleic acids with correlative single-cell imaging. *Nature Protocols*, *16*(1), 383–404.

Liu, Z., Lin, K. S., Bénard, F., Pourghiasian, M., Kiesewetter, D. O., Perrin, D. M., & Chen, X. (2015). One-step ^{18}F labeling of biomolecules using organotrifluoroborates. *Nature Protocols*, *10*, 1423–1432.

Maeda, H. (2001). The enhanced permeability and retention (EPR) effect in tumor vasculature: the key role of tumor-selective macromolecular drug targeting. *Advances in Enzyme Regulation*, *41*(1), 189–207.

Maschauer, S., Einsiedel, J., Haubner, R., Hocke, C., Ocker, M., Hübner, H., Kuwert, T., Gmeiner, P., & Prante, O. (2010). Labeling and Glycosylation of Peptides Using Click Chemistry: A General Approach to ^{18}F-Glycopeptides as Effective Imaging Probes for Positron Emission Tomography. *Angewandte Chemie International Edition*, *49*(5), 976–979.

McBride, W. J., D'souza, C. A., Sharkey, R. M., Karacay, H., Rossi, E. A., Chang, C. H., & Goldenberg, D. M. (2010). Improved ^{18}F labeling of peptides with a fluoride-aluminum- chelate complex. *Bioconjugate Chemistry*, *21*(7), 1331–1340.

McBride, W. J., Sharkey, R. M., & Goldenberg, D. M. (2013). Radiofluorination using aluminum-fluoride (Al[18]F). *EJNMMI Research*, *3*(1), 1–11.

McBride, W. J., Zanzonico, P., Sharkey, R. M., Norén, C., Karacay, H., Rossi, E. A., Losman, M. J., Brard, P. Y., Chang, C. H., Larson, S. M., & Goldenberg, D. M. (2006). Bispecific antibody pretargeting PET (ImmunoPET) with an 124I-labeled hapten-peptide. *Journal of Nuclear Medicine*, *47*(10), 1678–1688.

Meldal, M., & Diness, F. (2020). Recent Fascinating Aspects of the CuAAC Click Reaction. *Trends in Chemistry*, *2*(6), 569–584.

Meyer, J. P., Houghton, J. L., Kozlowski, P., Abdel-Atti, D., Reiner, T., Pillarsetty, N. V. K., Scholz, W. W., Zeglis, B. M., & Lewis, J. S. (2016). ^{18}F-Based Pretargeted PET Imaging Based on Bioorthogonal Diels-Alder Click Chemistry. *Bioconjugate Chemistry*, *27*(2), 298–301.

Meyer, J. P., Kozlowski, P., Jackson, J., Cunanan, K. M., Adumeau, P., Dilling, T. R., Zeglis, B. M., & Lewis, J. S. (2017). Exploring Structural Parameters for Pretargeting Radioligand Optimization. *Journal of Medicinal Chemistry*, *60*(19), 8201–8217.

Miller, C. M., Donner, A. J., Blank, E. E., Egger, A. W., Kellar, B. M., Østergaard, M. E., Seth, P. P., & Harris, E. N. (2016). Stabilin-1 and Stabilin-2 are specific receptors for the cellular internalization of phosphorothioate-modified antisense oligonucleotides (ASOs) in the liver. *Nucleic Acids Research*, *44*(6), 2782–2794.

Mirkin, C. A., Letsinger, R. L., Mucic, R. C., & Storhoff, J. J. (1996). A DNA-based method for rationally assembling nanoparticles into macroscopic materials. *Nature*, *382*, 607–609.

Mokhtarzadeh, A., Vahidnezhad, H., Youssefian, L., Mosafer, J., Baradaran, B., & Uitto, J. (2019). Applications of Spherical Nucleic Acid Nanoparticles as Delivery Systems. *Trends in Molecular Medicine*, *25*(12), 1066–1079.

Namavari, M., Cheng, Z., Zhang, R., De Abhijit, Levi, J., Hoerner, J. K., Yaghoubi, S. S., Syud, F. A., & Gambhir, S. S. (2009). A novel method for direct site-specific radiolabeling of peptides using [^{18}F]FDG. *Bioconjugate Chemistry*, *20*(3), 432–436.

Newton-Northup, J. R., Figueroa, S. D., Quinn, T. P., & Deutscher, S. L. (2009). Bifunctional phage-based pretargeted imaging of human prostate carcinoma. *Nuclear Medicine and Biology*, *36*(7), 789–800.

Oliveira, B. L., Guo, Z., & Bernardes, G. J. L. (2017). Inverse electron demand Diels-Alder reactions in chemical biology. *Chemical Society Reviews*, *46*(16), 4895–4950.

Orlovskaya, V., Fedorova, O., Nadporojskii, M., & Krasikova, R. (2019). A fully automated azeotropic drying free synthesis of O-(2-[^{18}F]fluoroethyl)-l-tyrosine ([^{18}F]FET) using tetrabutylammonium tosylate. *Applied Radiation and Isotopes*, *152*, 135–139.

Oroujeni, M., Tano, H., Vorobyeva, A., Liu, Y., Vorontsova, O., Xu, T., Westerlund, K., Orlova, A., Tolmachev, V., & Karlström, A. E. (2022). Affibody-Mediated PNA-Based Pretargeted Cotreatment Improves Survival of Trastuzumab-Treated Mice Bearing HER2-Expressing Xenografts. *Journal of Nuclear Medicine*, *63*(7), 1046–1051.

Otaru, S., Paulus, A., Imlimthan, S., Kuurne, I., Virtanen, H., Liljenbäck, H., Tolvanen, T., Auchynnikava, T., Roivainen, A., Helariutta, K., Sarparanta, M., & Airaksinen, A. J. (2022). Development of [^{18}F]AmBF3 Tetrazine for Radiolabeling of Peptides: Preclinical Evaluation and PET Imaging of [^{18}F]AmBF3-PEG7-Tyr3-Octreotide in an AR42J Pancreatic Carcinoma Model. *Bioconjugate Chemistry*, *33*(7), 1393–1404.

Parker, N., Turk, M. J., Westrick, E., Lewis, J. D., Low, P. S., & Leamon, C. P. (2005). Folate receptor expression in carcinomas and normal tissues determined by a quantitative radioligand binding assay. *Analytical Biochemistry*, *338*(2), 284–293.

Rashidian, M., Keliher, E. J., Dougan, M., Juras, P. K., Cavallari, M., Wojtkiewicz, G. R., Jacobsen, J. T., Edens, J. G., Tas, J. M. J., Victora, G., Weissleder, R., & Ploegh, H. (2015). Use of ^{18}F-2-fluorodeoxyglucose to label antibody fragments for immuno-positron emission tomography of pancreatic cancer. *ACS Central Science*, *1*(3), 142–147.

Ray, A., & Nordén, B. (2000). Peptide nucleic acid (PNA): its medical and biotechnical applications and promise for the future. *The FASEB Journal*, *14*(9), 1041–1060.

Reardan, D. T., Meares, C. F., Goodwin, D. A., McTigue, M., David, G. S., Stone, M. R., Leung, J. P., Bartholomew, R. M., & Frincke, J. M. (1985). Antibodies against metal chelates. *Nature*, *316*(6025), 265–268.

Rong, J., Haider, A., Jeppesen, T. E., Josephson, L., & Liang, S. H. (2023). Radiochemistry for positron emission tomography. *Nature Communications*, *14*, 3257.

Rossin, R., Verkerk, P. R., Van Den Bosch, S. M., Vulders, R. C. M., Verel, I., Lub, J., & Robillard, M. S. (2010). In Vivo Chemistry for Pretargeted Tumor Imaging in Live Mice. *Angewandte Chemie International Edition*, *49*(19), 3375–3378.

Ruschkowski, M., Fogarasi, M., Fritz, B., & Hnatowich, D. J. (1997). Effect of endogenous biotin on the applications of streptavidin and biotin in mice. *Nuclear Medicine and Biology*, *24*(3), 263–268.

Sakahara, H., & Saga, T. (1999). Avidin–biotin system for delivery of diagnostic agents. *Advanced Drug Delivery Reviews*, *37*(1–3), 89–101.

Saxon, E., Armstrong, J. I., & Bertozzi, C. R. (2000). A "traceless" Staudinger ligation for the chemoselective synthesis of amide bonds. *Organic Letters*, *2*(14), 2141–2143.

Saxon, E., & Bertozzi, C. R. (2000). Cell surface engineering by a modified Staudinger reaction. *Science*, *287*(5460), 2007–2010.

Schmaljohann, J., Schirrmacher, E., Wängler, B., Wängler, C., Schirrmacher, R., & Guhlke, S. (2011). Fully automated SPE-based synthesis and purification of 2-[^{18}F]fluoroethyl-choline for human use. *Nuclear Medicine and Biology*, *38*(2), 165–170.

Şenk, A. M., İçhedef, Kılçar, A. Y., Uçar, E., Arı, K., Göksoy, D., Parlak, Y., Sayıt Bilgin, B. E., & Teksöz, S. (2018). One-step conjugation of glycylglycine with [^{18}F]FDG and a pilot PET imaging study. *Journal of Radioanalytical and Nuclear Chemistry*, *316*(2), 457–463.

Shinde, S. S., Maschauer, S., & Prante, O. (2021). Sweetening pharmaceutical radiochemistry by ^{18}F-fluoroglycosylation: Recent progress and future prospects. *Pharmaceuticals*, *14*(11), 1175.

Silvola, J. M. U., Li, X. G., Virta, J., Marjamäki, P., Liljenbäck, H., Hytönen, J. P., Tarkia, M., Saunavaara, V., Hurme, S., Palani, S., Hakovirta, H., Ylä-Herttuala, S., Saukko, P., Chen, Q., Low, P. S., Knuuti, J., Saraste, A., & Roivainen, A. (2018). Aluminum fluoride-18 labeled folate enables in vivo detection of atherosclerotic plaque inflammation by positron emission tomography. *Scientific Reports*, *8*(1), 972.

Simeonova, G., Todorov, B., & Lyubomirova, V. (2023). Method for indirect radiofluorination with [^{18}F]FDG by biorthogonal reaction. *The European Physical Journal Special Topics*, *232*(10), 1555–1562.

Sita, T. L., Kouri, F. M., Hurley, L. A., Merkel, T. J., Chalastanis, A., May, J. L., Ghelfi, S. T., Cole, L. E., Cayton, T. C., Barnaby, S. N., Sprangers, A. J., Savalia, N., James, C. D., Lee, A., Mirkin, C. A., & Stegh, A. H. (2017). Dual bioluminescence and near-infrared fluorescence monitoring to evaluate spherical nucleic acid nanoconjugate activity in vivo. *Proceedings of the National Academy of Sciences of the United States of America*, *114*(16), 4129–4134.

Soellner, M. B., Nilsson, B. L., & Raines, R. T. (2006). Reaction mechanism and kinetics of the traceless Staudinger ligation. *Journal of the American Chemical Society*, *128*(27), 8820–8828.

Solin, O., Bergman, J., Haaparanta, M., & Reissell, A. (1988). Production of ^{18}F from water targets. Specific radioactivity and anionic contaminants. *International Journal of Radiation Applications and Instrumentation. Part A. Applied Radiation and Isotopes*, *39*(10), 1065–1071.

Soriano Del Amo, D., Wang, W., Jiang, H., Besanceney, C., Yan, A. C., Levy, M., Liu, Y., Marlow, F. L., & Wu, P. (2010). Biocompatible copper(I) catalysts for in vivo imaging of glycans. *Journal of the American Chemical Society*, *132*(47), 16893–16899.

Stéen, E. J. L., Edem, P. E., Nørregaard, K., Jørgensen, J. T., Shalgunov, V., Kjaer, A., & Herth, M. M. (2018). Pretargeting in nuclear imaging and radionuclide therapy: Improving efficacy of theranostics and nanomedicines. *Biomaterials*, *179*, 209–245.

Svatunek, D., Wilkovitsch, M., Hartmann, L., Houk, K. N., & Mikula, H. (2022). Uncovering the Key Role of Distortion in Bioorthogonal Tetrazine Tools That Defy the Reactivity/Stability Trade-Off. *Journal of the American Chemical Society*, *144*(18), 8171–8177.

Torchilin, V. (2011). Tumor delivery of macromolecular drugs based on the EPR effect. *Advanced Drug Delivery Reviews*, *63*(3), 131–135.

Tornøe, C. W., Christensen, C., & Meldal, M. (2002). Peptidotriazoles on solid phase: [1,2,3]-triazoles by regiospecific copper(I)-catalyzed 1,3-dipolar cycloadditions of terminal alkynes to azides. *Journal of Organic Chemistry*, *67*(9), 3057–3064.

Trump, L., Lemos, A., Lallemand, B., Pasau, P., Mercier, J., Lemaire, C., Luxen, A., & Genicot, C. (2019). Late-Stage ^{18}F-Difluoromethyl Labeling of N-Heteroaromatics with High Molar Activity for PET Imaging. *Angewandte Chemie International Edition*, *58*(37), 13149–13154.

Tsoi, K. M., Macparland, S. A., Ma, X. Z., Spetzler, V. N., Echeverri, J., Ouyang, B., Fadel, S. M., Sykes, E. A., Goldaracena, N., Kaths, J. M., Conneely, J. B., Alman, B. A., Selzner, M., Ostrowski, M. A., Adeyi, O. A., Zilman, A., McGilvray, I. D., & Chan, W. C. W. (2016). Mechanism of hard-nanomaterial clearance by the liver. *Nature Materials*, *15*(11), 1212–1221.

Van Der Born, D., Pees, A., Poot, A. J., Orru, R. V. A., Windhorst, A. D., & Vugts, D. J. (2017). Fluorine-18 labelled building blocks for PET tracer synthesis. *Chemical Society Reviews*, *46*(15), 4709–4773.

Wang, Z. P. A., Tian, C. L., & Zheng, J. S. (2015). The recent developments and applications of the traceless-Staudinger reaction in chemical biology study. *RSC Advances*, *5*(130), 107192–107199.

Welch, A., Tavares, A. A. S., Pimlott, S., & Sutherland, A. (2021). PET and SPECT in Drug Development. In *Burger's Medicinal Chemistry and Drug Discovery* (pp. 1–18). Wiley.

Wong, K. P., Sha, W., Zhang, X., & Huang, S. C. (2011). Effects of administration route, dietary condition, and blood glucose level on kinetics and uptake of ^{18}F-FDG in mice. *Journal of Nuclear Medicine*, *52*(5), 800–807.

Wright, J. S., Kaur, T., Preshlock, S., Tanzey, S. S., Winton, W. P., Sharninghausen, L. S., Wiesner, N., Brooks, A. F., Sanford, M. S., & Scott, P. J. H. (2020). Copper-mediated late-stage radiofluorination: five years of impact on preclinical and clinical PET imaging. *Clinical and Translational Imaging*, *8*(3), 167–206.

Wuest, F., Hultsch, C., Berndt, M., & Bergmann, R. (2009). Direct labelling of peptides with 2-[^{18}F]fluoro-2-deoxy-d-glucose ([^{18}F]FDG). *Bioorganic and Medicinal Chemistry Letters*, *19*(18), 5426–5428.

Zheng, Q., Xu, H., Wang, H., Du, W. G. H., Wang, N., Xiong, H., Gu, Y., Noodleman, L., Sharpless, K. B., Yang, G., & Wu, P. (2021). Sulfur [^{18}F]Fluoride Exchange Click Chemistry Enabled Ultrafast Late-Stage Radiosynthesis. *Journal of the American Chemical Society*, *143*(10), 3753–3763.

Äärelä, A., Auchynnikava, T., Moisio, O., Liljenbäck, H., Andriana, P., Iqbal, I., Lehtimäki, J., Rajander, J., Salo, H., Roivainen, A., Airaksinen, A. J., & Virta, P. (2023). In Vivo Imaging of [60]Fullerene-Based Molecular Spherical Nucleic Acids by Positron Emission Tomography. *Molecular Pharmaceutics*, *20*(10), 5043–5051.

**TURUN
YLIOPISTO
UNIVERSITY
OF TURKU**